# Design and Electrochemical Mechanism of the MgF$_2$ Coating as a Highly Stable and Conductive Interlayer on the Si Anode for High-Performance Li-Ion Batteries

*Shixiong Mei, Ben Xiang, Siguang Guo, Jiaguo Deng, Jijiang Fu, Xuming Zhang, Yang Zheng, Biao Gao,\* Kaifu Huo,\* and Paul K Chu*

**Silicon (Si) with high specific capacity, abundant reserve, and low cost is a promising replacement for graphite in anodes of next-generation lithium-ion batteries (LIBs). However, practical implementation is still hampered by the poor rate performance and short lifespan due to the unstable electrode/electrolyte interface and low ion/electron conductivity. Therefore, design of a stable and high-conductivity interface for Si anodes is desirable albeit challenging. Herein, a mixed ion/electron conducting interlayer (MIECI) consisting of LiF and Li–Mg alloy is formed in situ from an intermediate MgF$_2$ layer on the surface of the porous Si electrode in the first lithiation step to produce a robust solid electrolyte interface (SEI). The MIECI formation mechanism is investigated by *operando* Raman scattering, X-ray diffraction, and Fourier transform infrared spectroscopy. LiF in the MIECI provides high ion conductivity, while the Li–Mg alloy produces fast electron conductivity and high mechanical strength. As a result, the p-Si@MgF$_2$ anode shows excellent cycling stability with 90% capacity retention after 200 cycles and a superior rate capacity of 70% when the current density is increased from 0.5 to 5.0 A g$^{-1}$. The novel interfacial modification and engineering strategy has large potential in the design and fabrication of Si anodes for LIBs.**

## 1. Introduction

Silicon (Si) based anode materials are attractive alternatives to commercial graphite anodes in lithium-ion batteries (LIBs) due to the increasing demand for 3 C products and electric vehicles (EVs) (> 600 km). Although Si has a theoretical specific capacity (4200 mAh g$^{-1}$) and low electrochemical potential (< 0.4 V),[1–6] Si anodes are prone to aging, capacity fading, and impedance increase in practice.[7,8] Furthermore, there are problems associated with the solid-electrolyte interphase (SEI) and

"dead" Li–Si alloy due to large volume change and inferior electrolyte/electrode interface.[9,10] Therefore, designing a stable SEI with high mechanical strength and enhanced electron/ion conductivity on Si anodes is crucial to the development of Si anodes for high-performance LIBs.[11,12]

One of the popular theories about SEI is the "mosaic model", in which the SEI consists of multiple organic and inorganic layers.[13,14] In mainstream carbonate-based electrolytes, the outer organic species are composed of high-oxidation-state organic and polymeric compounds such as ROCO$_2$Li and (ROCO$_2$Li)$_2$. These substances originate from the side reactions of the highly catalytic lithium and organic carbon polymers and often show low elastic modulus and poor conductivity. Although the inorganic components near the electrode including Li$_2$O, Li$_2$CO$_3$, and LiF have better ionic conductivity and electrochemical stability for the SEI,[15] they are still plagued by the low electron conductivity and high brittleness. Moreover, their distributions are typically nonuniform leading to inhomogeneous Li-ion diffusion in the SEI layer. Several strategies have been proposed to improve the quality of the SEI on Si anodes.[16–19] For example, some electrolyte additives such as fluoroethylene carbonate (FEC)[20] and vinylene carbonate (VC)[21] have been used to produce LiF-rich protective layers in situ and create a buffer between the active materials and electrolyte.[22] Unfortunately, formation of LiF is the main reason for electrode pulverization and capacity loss on

S. Mei, B. Xiang, S. Guo, J. Deng, J. Fu, X. Zhang, Y. Zheng, B. Gao
The State Key Laboratory of Refractories and Metallurgy
and Institute of Advanced Materials and Nanotechnology
Wuhan University of Science and Technology
Wuhan 430081, China
E-mail: gaobiao@wust.edu.cn

K. Huo
Wuhan National Laboratory for Optoelectronics (WNLO)
School of Optical and Electronic Information
Huazhong University of Science and Technology
Wuhan 430074, China
E-mail: kfhuo@hust.edu.cn

P. K. Chu
Department of Physics
Department of Materials Science & Engineering, and Department of Biomedical Engineering
City University of Hong Kong
83 Tat Chee Avenue, Kowloon, Hong Kong 518057, China

The ORCID identification number(s) for the author(s) of this article can be found under https://doi.org/10.1002/adfm.202301217.
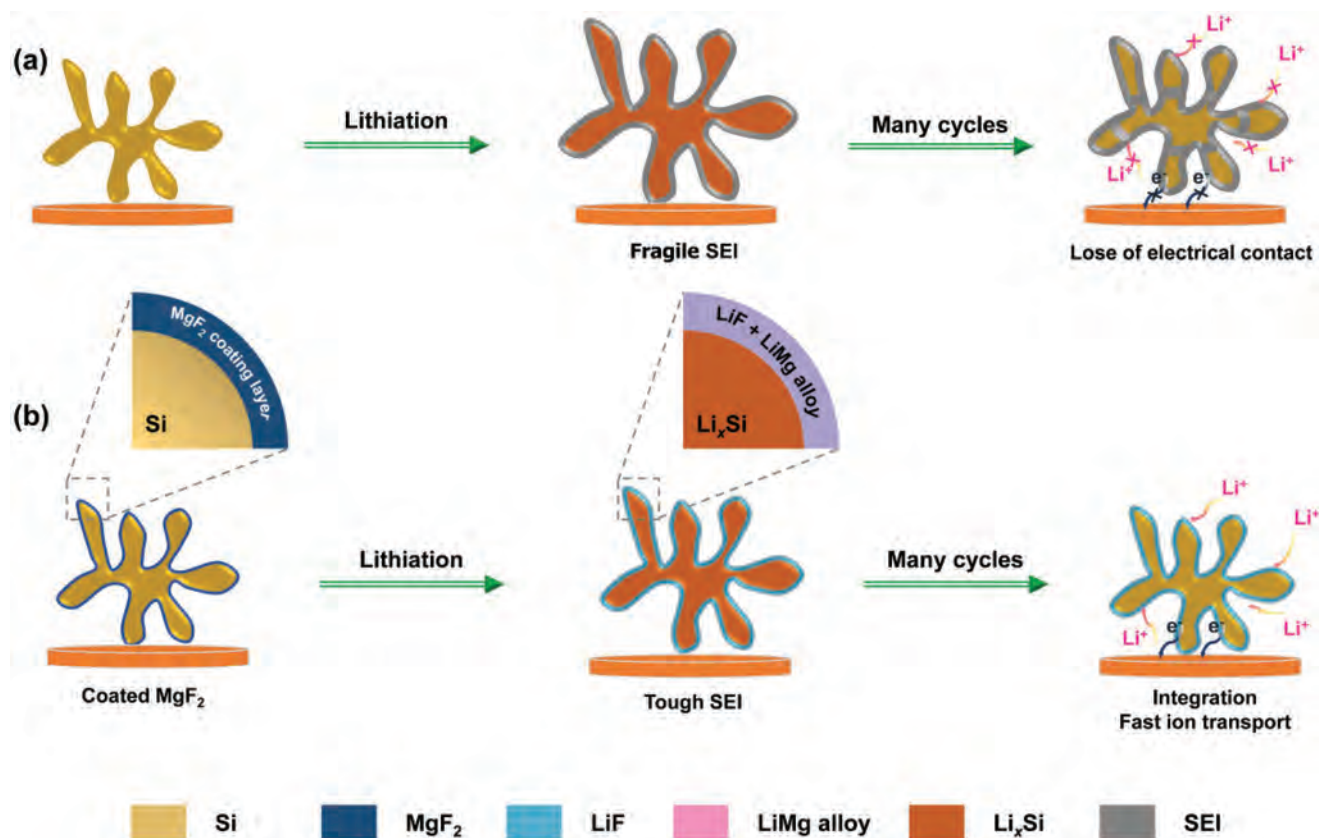
DOI: 10.1002/adfm.202301217

**Figure 1.** Schematic illustration of a) p-Si particle and b) $MgF_2$ surface modification on p-Si particles during lithiation and cycling as anode materials for LIBs.

account of the poor electrical conductivity and brittle nature.[23] A surface coating can assist in the formation of a stable and conductive LiF-rich SEI to enhance the electrochemical properties.[24–27] For instance, Peng et al. have synthesized a conformal LiF layer as an artificial SEI coating on the Si nanocolumn anode to obtain the superior rate capability and cycling stability because LiF increases the $Li^+$ diffusion coefficient (LDC).[28] However, LiF-based inorganic coatings with low electron conductivity and high fragility can result in a discontinuous and cracked SEI. The desirable LiF based SEI for Si-based anodes must overcome the disadvantages of electron conductivity and mechanical fragility while exhibiting high electro-chemical stability, electronic/ionic conductivity, as well as good toughness.

Herein, a mixed ion/electron conducting interlayer (MIECI) consisting of LiF and Li–Mg alloy is formed in situ from an intermediate $MgF_2$ layer on the surface of the porous Si electrode (denoted as p-Si@$MgF_2$). The structure evolution processes of the p-Si and p-Si@$MgF_2$ anode are depicted in **Figure 1**. As shown in Figure 1a, the skeleton of p-Si will expand and generate a fragile SEI during the first lithiation. Upon following cycling, the SEI easily breaks down due to low toughness and becomes thicker because of continuous growth, resulting in loss of electrical contact and fast capacity decay. Figure 1b illustrates the evolution mechanism of the $MgF_2$ coating layer in enhancing interfacial conductivity and stability. In the initial lithiation, a tough SEI with high ion/electron conductivity consisting of LiF and Li–Mg alloy is converted from

$MgF_2$. LiF not only has a high Li ion conductivity, but also contributes to constructing a LiF-rich SEI, which enabling a stable and Li ion conductive interface. While the Li–Mg has a high toughness and electron conductivity, leading to enhanced strength and electron conductivity. Thus, designing an artificial MIECI on porous Si via $MgF_2$ coating is predicted to improve the electrochemical performance of Si anodes. The electrochemical mechanism of the $MgF_2$-based coating and effects on the Li storage properties are unraveled by in situ analytical techniques. Compared to p-Si, better electrochemical characteristics such as a capacity of 942 mAh $g^{-1}$ at 5 A $g^{-1}$ are achieved from p-Si@$MgF_2$ due to the MIECI coating derived from $MgF_2$. Moreover, p-Si@$MgF_2$ exhibits outstanding battery cycling properties such as high-capacity retention of 90% and reversible capacity of 1403 mAh $g^{-1}$ after 200 cycles at 1 A $g^{-1}$.

## 2. Results and Discussion

### 2.1. Synthesis and Structural Characterization of p-Si@$MgF_2$

We have fabricated ant-nest-like porous Si particles via nitriding of $Mg_2Si$ and dissolving the nitriding product ($Mg_3N_2$/Si) in HCl.[4,29] p-Si@$MgF_2$ is synthesized by converting a small portion of Mg into $MgF_2$ in an aqueous solution during HCl etching (**Figure 2**a). The morphology and chemical composition of the samples after the heat treatment are shown in the TEM
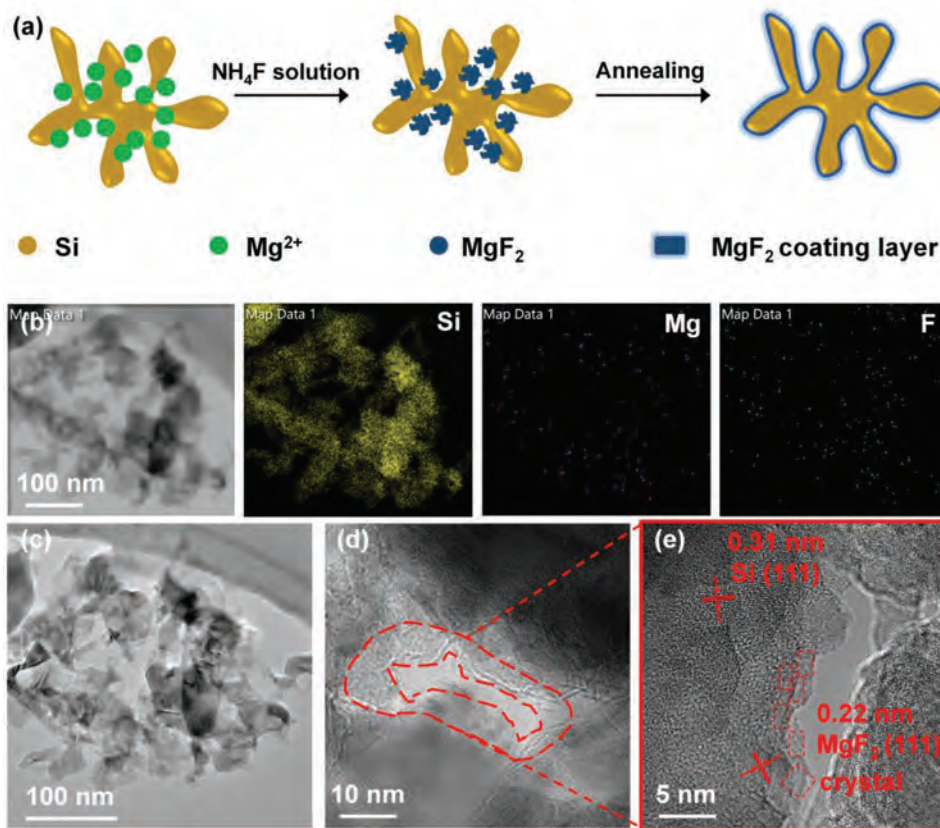
**Figure 2.** a) Schematic diagram of the preparation of p-Si@MgF$_2$; b) TEM image and elemental maps of Si, Mg, and F of p-Si@MgF$_2$; c) TEM, d) HR-TEM, and e) Partially magnified HR-TEM images of p-Si@MgF$_2$.

images and elemental maps (Figure 2b). The 3D interconnected Si nanoligaments and bicontinuous nanoporous network composed of Mg and F are dispersed on the surface of the Si network. The XRD patterns of p-Si@MgF$_2$, p-Si@MgF$_2$-1, and p-Si@MgF$_2$-2 in Figure S1a (Supporting Information) reveal broad diffraction peaks at 28.5 °, 47.3 °, 56.2 °, 69.2 °, and 76.5 ° associated with the (111), (220), (311), (400), and (331) planes of the cubic phase of Si (JCPDS No. 27–1402).[30] Other peaks are not observed from p-Si@MgF$_2$ because of the small MgF$_2$ concentration. However, further increase of the MgF$_2$ concentration produces a weak peak at 26 ° corresponding to the (100) plane of tetragonal MgF$_2$ (JCPDS No. 41–1443).[31,32] To further study the proportion of MgF$_2$ in the as-prepared samples, the XRD refinement date carried out (Figure S1b–d, Supporting Information) shows that the contents of MgF$_2$ in the p-Si@MgF$_2$, p-Si@MgF$_2$-1 and p-Si@MgF$_2$-2 samples are 0.2, 3.2 and 8.8 wt.%, respectively and the corresponding inductively-coupled plasma optical emission spectrometer (ICP-OES) results are listed in Table S1 (Supporting Information). The SEM images of p-Si, p-Si@MgF$_2$, p-Si@MgF$_2$-1, and p-Si@MgF$_2$-2 are depicted in Figure S2 (Supporting Information). p-Si@MgF$_2$ has an obvious porous structure and with increasing MgF$_2$ content, the porous structure blurs gradually as shown by the STEM images and elemental maps of Si, Mg, and F in Figure S3 (Supporting Information).

XPS is conducted to characterize the surface chemical composition of p-Si@MgF$_2$ before and after Ar ion etching (Figure S4, Supporting Information). Before Ar ion etching, a broad peak at 1305.0 eV in the XPS Mg 1$s$ spectrum stems from Mg$^{2+}$ and the peak at 686.8 eV in the F 1$s$ spectrum represents F$^-$ confirming the formation of MgF$_2$.[33] After Ar ion etching for 14 s at a sputtering rate of 0.5 nm s$^{-1}$, the Mg$^{2+}$ and F$^-$ peaks of p-Si@MgF$_2$ disappear but the Si peak emerges indicating that the thickness of the MgF$_2$ layer is less than 7 nm. The TEM image in Figure 2c shows that the ant-nest-like porous Si with a pore size of 50–100 nm forms 3D interconnected Si nanoligaments with a size of 10–30 nm. The HR-TEM images in Figure 2d,e disclose that the tetragonal MgF$_2$ nanocrystals with a diameter of ≈1–2 nm adhere to the surface of porous Si and the lattice spacing of 0.22 nm corresponds to (111) crystal plane of MgF$_2$,[34] which is different with the surface of p-Si (Figure S5, Supporting Information). The p-Si and p-Si@MgF$_2$ have similar specific surface areas, which are measured to be 53.6 and 53.5 m$^2$ g$^{-1}$, respectively (Figure S6, Supporting Information). The porosity of p-Si@MgF$_2$ is 0.43 cm$^3$ g$^{-1}$, which is slightly less than 0.49 cm$^3$ g$^{-1}$ of p-Si. These results indicate that the MgF$_2$ has a small influence on the surface area and pore volume due to the thin coating.

## 2.2. Lithiation Mechanism of MgF$_2$

To investigate the electrochemical properties and roles of MgF$_2$ on Si-based anodes, in situ XRD is performed on the
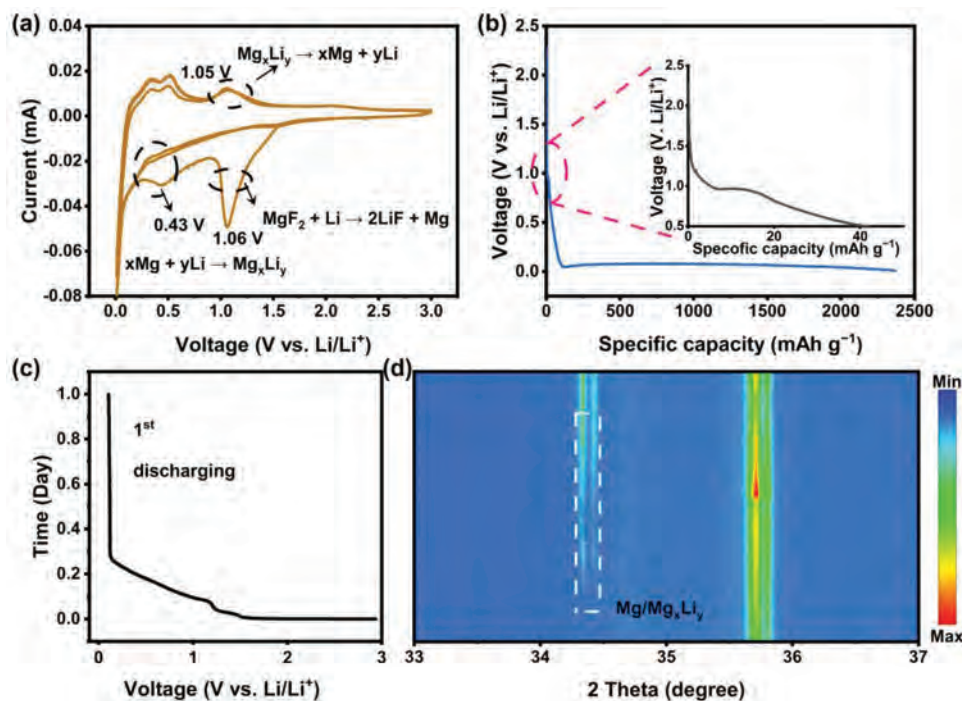
**ADVANCED
SCIENCE NEWS**
www.advancedsciencenews.com

**ADVANCED
FUNCTIONAL
MATERIALS**
www.afm-journal.de

**Figure 3.** a) CV curves of the p-Si@MgF$_2$-2 anode at 0.1 mV s$^{-1}$ from 0.01 to 3.0 V; b) GCD profile of the p-Si@MgF$_2$ anode at 0.1 A g$^{-1}$ with the inset showing the magnified region; c) Discharge profile at 20 mA g$^{-1}$ and d) Corresponding in situ XRD patterns of the p-Si@MgF$_2$-2 anode.

p-Si@MgF$_2$ anodes to characterize the phase change after initial lithiation. The in situ formation mechanism of the MIECI can be monitored by the CV curves and the initial discharge profiles. The CV curves of the p-Si@MgF$_2$-2 anode at 0.1 mV s$^{-1}$ show that compared to pure p-Si, a reduction peak is observed at 1.06 V from the p-Si@MgF$_2$-2 electrode (**Figure 3**a) indicating the irreversible conversion reaction of MgF$_2$ (MgF$_2$ + Li → 2 LiF + Mg). Another peak observed at a lower potential of 0.43 V contributes to the reversible alloying reaction (Mg + Li ⇌ Mg$_x$Li$_y$) to produce the Li–Mg alloy, while the peak at 1.05 V can be ascribed to dealloying of the Li–Mg alloy.[31] To in-depth study the reaction behavior of MgF$_2$, the CV curves of pure MgF$_2$ are tested at 0.1 mV s$^{-1}$ between 2.0 and 0.01 V with the Li foil as anode (Figure S7, Supporting Information). Accordingly, the plateau at 0.9–1.3 V of p-Si@MgF$_2$-2 in Figure 3b represents the lithiation reaction of MgF$_2$. To further elucidate the formation mechanism of MgF$_2$, in situ XRD is performed during discharging in an in situ XRD cell as displayed in Figure S8 (Supporting Information) and Figure 3c shows the first galvanostatic discharge curve at 20 mA g$^{-1}$ from 3.0 to 0.01 V. The in situ XRD pattern of the p-Si@MgF$_2$-2 anode in Figure 3d discloses a broad peak at 35.6 ° related to the body-centered cubic phase of the Li–Mg alloy (JCPDS No. 65–9347).[35] The fine XPS spectra of Mg 1$s$ of the p-Si@MgF$_2$-2 anode are obtained before and after the first cycle in Figure S9 (Supporting Information). There are two peaks located at 1303.7 and 1304.5 eV corresponding to Mg–Mg/Li–Mg (converted Mg metal and untransformed Li–Mg alloy) bonds and Mg$^{2+}$ (residual MgF$_2$),[33] which clarifies that Mg$_x$Li$_y$ has transformed into Mg and Li after the first cycle. These results show that the MIECI is formed in situ on the Si anode after initial lithiation.

### 2.3. Corrosion Resistance of MIECI in the Electrolyte

Contact angle and in situ FTIR analyses are carried out to assess the decomposition process of the electrolyte and corrosion resistance of the Si-based electrode. As shown in **Figure 4**a,b, the contact angle on the p-Si@MgF$_2$ electrode is 24.0 ° at t = 0 s, which is larger than 19.5 ° of the p-Si electrode in the electrolyte. After 29 s, the p-Si@MgF$_2$ electrode still shows a small contact angle of 4.5 ° but the liquid electrolyte covers the p-Si electrode entirely after 6 s. Hence, the MgF$_2$ coating layer retards electrolyte penetration and better separates the electrolyte from the Si core to decrease the side reactions in the electrolyte. Electrolyte decomposition for the p-Si@MgF$_2$ and p-Si anodes is monitored by in situ FTIR (Figure 4c,d) in the first CV cycle at 0.1 mV s$^{-1}$ (Figure S10, Supporting Information). CO$_2$, originating from a reaction between lithium alkyl carbonate either and HF or water in the electrolyte can be used to evaluate electrolyte decomposition and corrosion resistance of the electrode.[36] The peak at 2300–2400 cm$^{-1}$ corresponds to CO$_2$ formed from the reaction between the electrode and electrolyte. Compared to pristine p-Si, the appearance of CO$_2$ from the p-Si@MgF$_2$-based cell is later than that of the p-Si anode, indicating that the MgF$_2$ coating remits the reaction between HF and SEI.

### 2.4. Electrochemical and Kinetic Properties

**Figure 5**a presents the cycling characteristics of the p-Si@MgF$_2$ and p-Si anodes at 1.0 A g$^{-1}$ after activation for three cycles at 0.1 A g$^{-1}$. The p-Si@MgF$_2$ anode (discharge capacity
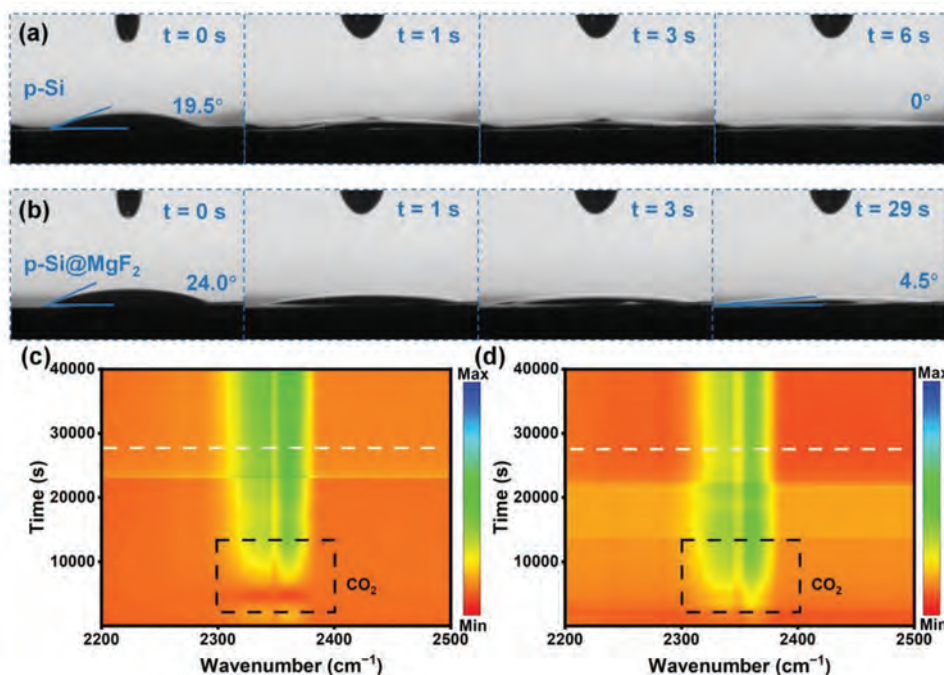
**Figure 4.** Corrosion resistance of the p-Si@MgF$_2$ and p-Si anodes. Dynamic contact angles on a) p-Si and b) p-Si@MgF$_2$; In situ FTIR spectra of c) p-Si@MgF$_2$ anode and d) p-Si anode of the initial CV cycle at 0.1 mV s$^{-1}$.

of 2894 mAh g$^{-1}$ (Figure S11, Supporting Information) indicates that the suitable MgF$_2$ coating has little effect on the capacity of Si. The initial Columbic efficiency of p-Si@MgF$_2$ is slightly less than that of p-Si because of the irreversible conversion reaction between MgF$_2$ and Li ions to form LiF and Li–Mg on the anodes. In comparison, the p-Si@MgF$_2$ anode exhibits a discharge capacity of 1600 mAh g$^{-1}$ with 90% capacity retention calculated from the 4th to 200th cycles at a current density of 1.0 A g$^{-1}$ and it is larger than that of the p-Si anode (60%). The rate capabilities of the p-Si@MgF$_2$ and p-Si anodes are monitored at different current densities between 0.1 and 5.0 A g$^{-1}$ before returning to 0.1 A g$^{-1}$, as shown in Figure 5b and Figure S12 (Supporting Information). Although the p-Si anode offers relatively high specific capacities at low current densities, the p-Si@MgF$_2$ anode shows high-capacity retention of 70% (942 mAh g$^{-1}$) when the current is increased 50 times from 0.1 to 5.0 A g$^{-1}$, which is better than that of p-Si and most of the literature reported about Si anodes (Table S2, Supporting Information). Even when the current density is reverted back to 0.1 A g$^{-1}$, the p-Si@MgF$_2$ anode still exhibits superior capacity retention (100%) indicative of high reversibility. The p-Si@MgF$_2$/Graphite | LFP full cell shows a discharge capacity of 149.5 mAh g$^{-1}$ and a high ICE of 86.2% at 0.1 C (1.0 C = 170.0 mAh g$^{-1}$), and charge capacity of 90 mAh g$^{-1}$ after 160 cycles at 1.0 C (Figure S13, Supporting Information), demonstrating the promising potential for practical applications.

The electrochemical enhancement mechanism of p-Si with the aid of MIECI is investigated by analyzing the differential discharge capacity curves of the p-Si and p-Si@MgF$_2$ anodes for 200 cycles (Figure 5c,d). Initially, the p-Si@MgF$_2$ anode shows a differential capacity peak near 0.25 V, which is lower than that of the p-Si anode (0.32 V) and consistent with the CV curves

reflecting good reversibility and fast Li ion transfer kinetics.[37] The peak of the p-Si anode shifts from 0.32 to 0.22 V from the 1st to 200th cycles implying large polarization. Compared to p-Si, the peak position of p-Si@MgF$_2$ is relatively constant showing only a small shift representing smaller polarization and faster Li ions transfer. The CV curves of p-Si@MgF$_2$ and p-Si at 0.1 mV s$^{-1}$ from the 5th to 10th cycles are displayed in Figure S14 (Supporting Information) in which A1 is the anodic peak of Si and C1 and C2 correspond to the cathodic peaks of Si, respectively. From the 5th to 10th cycle, the A1, C1 and C2 peaks of the p-Si@MgF$_2$ remain at 0.201, 0.373, and 0.518 V, respectively, but the A1 (0.189 to 0.122 V), C1 (0.383 to 0.419 V), and C2 (0.533 to 0.588 V) peaks of the p-Si shift significantly. The p-Si electrode exhibits more severe polarization than the p-Si@MgF$_2$ electrode in agreement with the differential discharge capacities.

To further study the effects of the MIECI on the Li storage properties of Si, in situ Raman scattering is performed during the 2nd CV cycle at 0.1 mV s$^{-1}$. As shown in Figure 5e,f, the peak 400–650 cm$^{-1}$ represents the shift of elemental Si and the concentration is reflected by the color intensity. The Si concentration in the p-Si@MgF$_2$ anode is larger than that in p-Si after the 1st lithiation/delithiation cycle implying less residual Li$_x$Si and higher reversibility of p-Si@MgF$_2$. As the voltage is reduced in the 2nd lithiation step, the intensity of the Raman peak of Si weakens gradually and even disappears from the p-Si and p-Si@MgF$_2$ anodes, demonstrating that Si is transformed into Li$_x$Si. The Si peak appears step by step during the 2nd delithiation cycle representing the de-alloying of Li$_x$Si. The highest Si intensity emerges earlier from the p-Si@MgF$_2$ electrode with a lower de-alloying potential than p-Si. The results reveal that the p-Si@MgF$_2$ anode has a larger lithiation
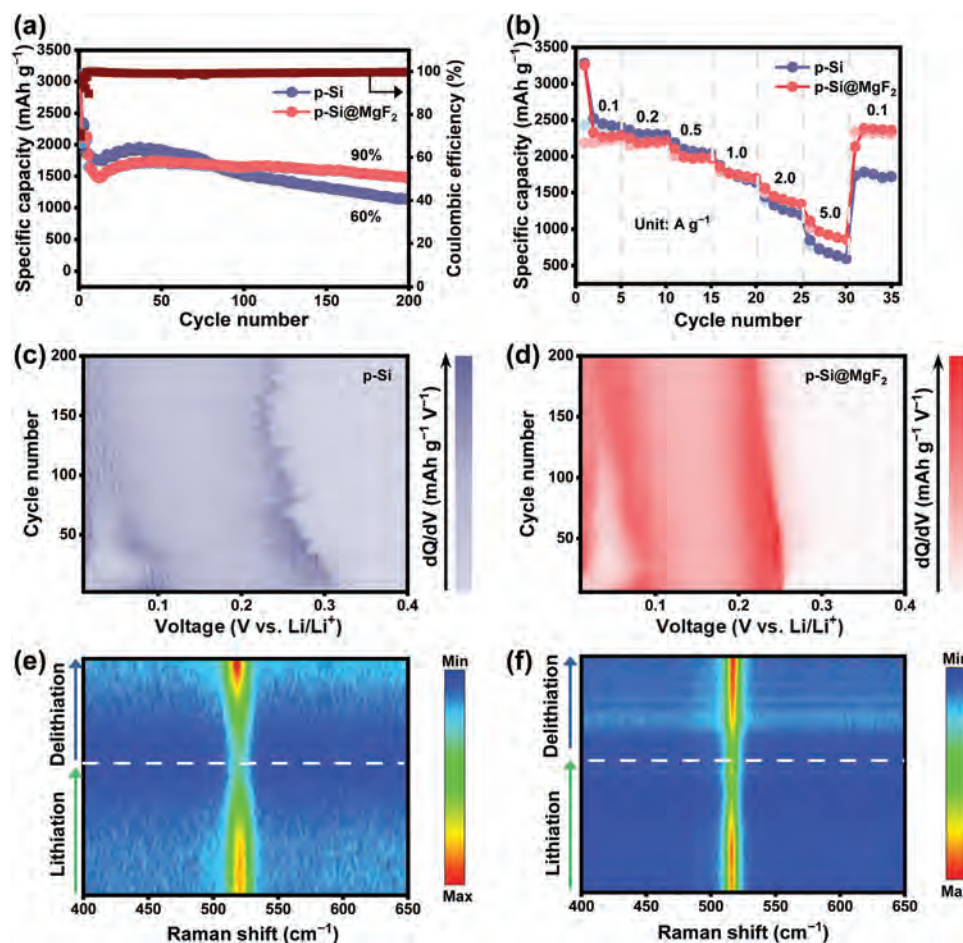
**Figure 5.** Electrochemical properties of p-Si@MgF$_2$ and p-Si. a) Cycling characteristics and b) Rate capabilities of the p-Si@MgF$_2$ and the p-Si anodes; Contour maps of differential capacity (d$Q$/d$V$) versus voltage of c) p-Si and d) p-Si@MgF$_2$ anodes for 200 cycles; Corresponding *operando* Raman scattering spectra of e) p-Si and f) p-Si@MgF$_2$ of the 2nd CV cycle at 0.1 mV s$^{-1}$.

rate and better reversibility. All in all, the in situ results indicate that the MIECI generated from MgF$_2$ plays an important role in inhibiting decomposition of the electrolyte and accelerating electron/ion transport during lithiation/delithiation.

Figure S15a,b (Supporting Information) show the EIS profiles and fitted resistances of the p-Si and p-Si@MgF$_2$ anodes after different cycles (Figure S15c, Supporting Information). The SEI resistance ($R_{SEI}$) of the p-Si@MgF$_2$ anode is smaller than that of the p-Si anode, meaning that the MIECI contributes to faster electron/ion interface transport. The electrochemical kinetics of the p-Si and p-Si@MgF$_2$ anode after 10 cycles are determined based on the Nyquist plots at low frequencies. The lithium diffusion coefficient can be calculated by the following equations:[38]

$$D_{Li^+} = \left( R^2 T^2 \right) / \left( 2 A^2 n^4 F^4 C^2 \sigma^2 \right) \tag{1}$$

$$Z' = R_e + R_{ct} + \sigma \omega^{-1/2} \tag{2}$$

where $T$ is the absolute temperature, $R$ is the gas constant, $A$ is the surface area of the electrode, $n$ is the number of electrons transferred in the reaction, $F$ is Faraday's constant, and $C$ is the concentration of Li-ions in the electrode. The Li diffusion coefficient ($D_{Li^+}$) is inversely proportional to the Warburg factor ($\sigma$), which is correlated to Z′ aligned with the slope. $D_{Li^+}$ of the p-Si@MgF$_2$ anode is ≈3.7 times bigger than that of p-Si, indicating more prominent kinetics for the p-Si@MgF$_2$ anode in lithium-ion storage (Figure S15d, Supporting Information). To further investigate the Li ion storage mechanism of the p-Si@MgF$_2$ anode in LIBs, CV is performed at different scanning rates from 0.1 to 0.6 mV s$^{-1}$ (Figure S16a,b, Supporting Information). There are capacitive and diffusion contributions and the ratio can be calculated by Equation (3) and (4):[39]

$$i = a v^b \; (0.5 \leq b \leq 1) \tag{3}$$

and

$$\log i = b \log v + \log a \tag{4}$$

where $a$ is a coefficient, $i$ is the measured current, $v$ is the sweeping rate, $b = 0.5$ reveals a diffusion contribution process entirely, and $b = 1$ indicates a capacitive contribution process. A $b$ value between 0.5 and 1 suggests mixed diffusion and capacitive

**ADVANCED
SCIENCE NEWS**

www.advancedsciencenews.com

**ADVANCED
FUNCTIONAL
MATERIALS**

www.afm-journal.de

contributions. As shown in Figure S16c,d (Supporting Information), the *b* value at the peak potential of the cathodic reaction of p-Si@MgF$_2$ is 0.77, suggesting a mixed capacitive contribution for fast storage/release of Li$^+$ at high rates. Meanwhile, the EIS profiles and corresponding equivalent circuits after CV are acquired at different scanning rates as shown in Figures S17 and S18 (Supporting Information). As shown in Table S3 (Supporting Information), the fitted $R_{ct}$ and $R_{SEI}$ values of the Si@MgF$_2$ electrodes after cycling at different rates are smaller than those of the Si electrodes, further proving that the MgF$_2$ coating stabilizes the SEI on p-Si, reduces the electrode/electrolyte interface impedance, and provides uniform Li$^+$ and electron pathway by in situ formation of the MIECI.

## 2.5. Interfacial Chemical Composition and Distribution

The interfacial composition is important to the formation of a high-quality SEI and XPS depth profiling by Ar sputtering is performed to determine the chemical composition of the p-Si@MgF$_2$ and p-Si anodes after the 1st charge/discharge cycle. **Figure 6**a shows the high-resolution C 1*s* spectrum of the p-Si@MgF$_2$ and p-Si anodes before and after 10 nm sputtering.

The concentrations of C–C (284.6 eV) and C–O (286.2 eV) on the surface of both samples are similar,[40] but the concentration of CO$_3^{2-}$ of the p-Si@MgF$_2$ anode is less than that of p-Si, indicating less decomposition of EC and DEC for p-Si@MgF$_2$. The high-resolution F 1*s* spectrum of p-Si@MgF$_2$ (Figure 6b) before Ar sputtering shows two peaks at 684.7 and 686.5 eV from the generated LiF and residual MgF$_2$, respectively. After sputtering for 10 nm, the MgF$_2$ phase disappears and the peak intensity of LiF is still intense and 5 times higher than that of the p-Si electrode, indicating the formation of the LiF-rich SEI on the p-Si@MgF$_2$ electrode. Besides the LiF phase, a broad peak at 688.7 eV emerging from the p-Si electrode can be ascribed to isolation of C–F bonds due to electrolyte decomposition. As shown in Figure 6c, in addition to the Li$_x$Si$_y$O$_z$ peak (101.6 eV), another peak at 97.5 eV stems from the Li$_x$Mg$_y$Si$_z$ ternary Zintl phase.[41] Formation of the Li–Mg–Si ternary Zintl phase boosts mechanical strength and electron conductivity. It not only improves the quality of the SEI but also enhances the rate performance of the p-Si anode.[42] As schematically shown in Figure 6d,e, while a loose and thick SEI with more organic species is generated on the p-Si electrode, a stable and thin SEI with LiF-rich species can be found on the p-Si@MgF$_2$ electrode after initial lithiation due to MgF$_2$.
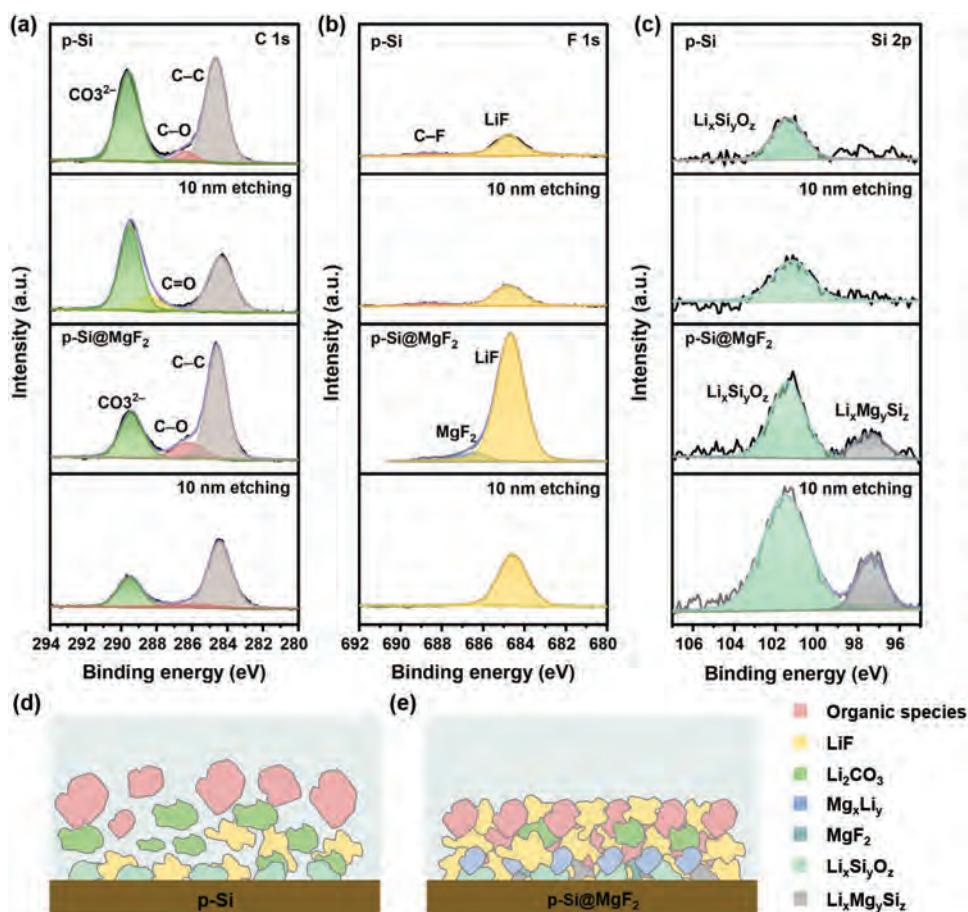


**Figure 6.** High-resolution XPS spectra of a) C 1s, b) F 1s, and c) Si 2p of the p-Si and p-Si@MgF$_2$ anodes after Ar ion sputtering for different time after the first cycle; Schematic illustration of the SEI structure formed on d) p-Si and e) p-Si@MgF$_2$.
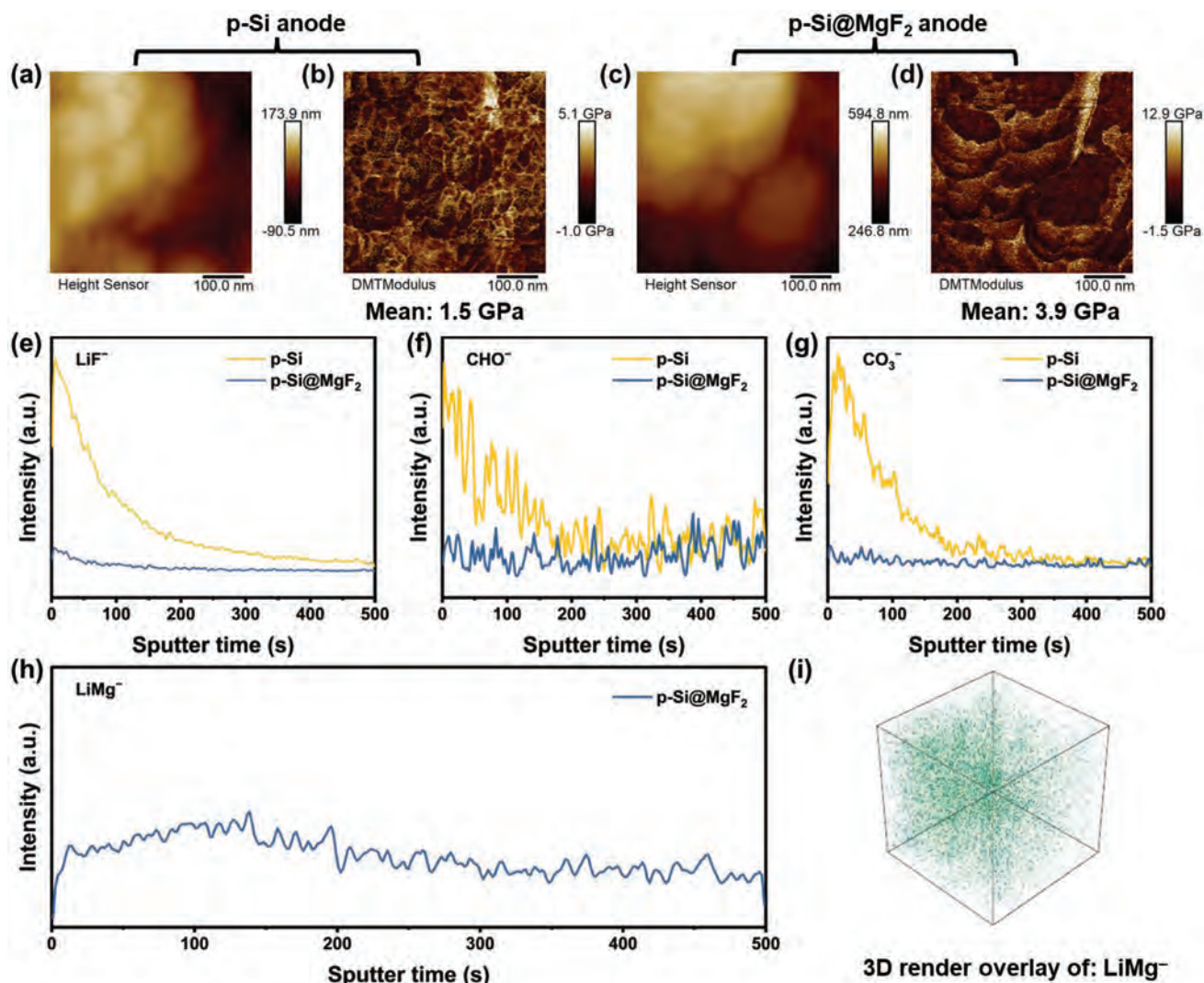
**Figure 7.** Mechanical strength and chemical composition of SEI of the p-Si@MgF$_2$ anode and p-Si anode. Surface morphology and moduli derived by AFM of the p-Si@MgF$_2$ and p-Si anodes after 10 cycles in comparison with a,c) p-Si and b,d) p-Si@MgF$_2$; ToF-SIMS spectra at different sputtered depths: e) LiF$^-$, f) CHO$^-$, and g) CO$_3^-$ of the p-Si and the p-Si@MgF$_2$ anodes after 10 cycles; h) ToF-SIMS depth profiles and i) 3D distribution of LiMg$^-$ are collected on p-Si@MgF$_2$.

## 2.6. Mechanical Properties and Structure of SEI During Cycling

To study the effects of the MIECI on the mechanical properties of SEI, the Young's moduli of the p-Si@MgF$_2$ and p-Si anodes after 10 cycles are determined by a surface force mapping technique with high spatial resolution using the Quantitative Nano mechanical (QNM) AFM. The modulus of the p-Si@MgF$_2$ anode is 3.9 GPa and much larger than that of the p-Si anode (1.5 GPa), as shown in **Figure 7**a–d. Therefore, the formation of the MIECI with strong bonding enhances the mechanical properties of the SEI of the p-Si@MgF$_2$ electrode and also restrains the generation of internal cracks during cycling to improve cycling stability.

Time-of-flight secondary ion mass spectrometry (ToF-SIMS) is conducted to monitor the chemical evolution of the p-Si@MgF$_2$ and p-Si anodes after 5 cycles. As shown in Figure S19 (Supporting Information), the main ions of the SEI such as

LiF$^-$, CHO$^-$, and CO$_3^-$ are observed (Figure S20, Supporting Information), indicating that the total organic and inorganic substances in p-Si are more than those in p-Si@MgF$_2$. Therefore, the total SEI film of p-Si@MgF$_2$ is less than that of p-Si, which is also confirmed by the LiF$^-$, CHO$^-$, and CO$_3^-$ concentrations at different sputtered depths (sputtering time of 0–500 s) (Figure 7e–g). Moreover, the ToF-SIMS spectra and corresponding 3D distributions of LiMg$^-$ (Figure 7h,i) acquired from the surface of p-Si@MgF$_2$ illustrate that LiMg$^-$ is uniformly distributed in the whole electrode. Hence, the MIECI inhibits the decomposition of the electrolyte and growth of the SEI on the p-Si@MgF$_2$ anode surface consistent with in situ FTIR.

To further explain the superiority of the MIECI with respect to the structure and morphology of the electrode, the p-Si, and the p-Si@MgF$_2$ electrodes are investigated after 200 cycles. Obvious fracture and delamination are observed from the p-Si

electrode after cycling (Figure S21a, Supporting Information) but on the other hand, the surface of the p-Si@MgF$_2$ electrode is still smooth showing no visible cracks or materials loss (Figure S21b, Supporting Information). Moreover, there is no obvious increase in the surface roughness on the p-Si@MgF$_2$ electrode (Figure S22, Supporting Information) according to the AFM 3D morphology images of the p-Si@MgF$_2$ electrode before and after cycling, further confirming the high mechanical robustness and stable interface.

## 3. Conclusion

A green and sustainable strategy is demonstrated for the construction of a mixed ion/electron conducting interlayer (MIECI) consisting of LiF and Li–Mg alloy derived by an intermediary MgF$_2$ layer on porous Si. In situ XRD, Raman scattering, and FTIR reveal the conversion mechanism from MgF$_2$ to LiF/Li–Mg and concomitant positive effects on the lithiation kinetics of the p-Si anode together with inhibition of electrolyte decomposition. The outstanding electrochemical properties of the MIECI lead to the formation of a thin and stable LiF-rich SEI with high electro-mechanical robustness and high ion/ electron conductivity. It can withstand the large strain from the large volume change during cycling and inhibit electrolyte over-decomposition. As a result, the p-Si@MgF$_2$ anode shows excellent and stable cycling characteristics manifested by high-capacity retention of 90%, reversible capacity of 1403 mAh g$^{-1}$ after 200 cycles at 1.0 A g$^{-1}$, capacity retention of 70%, as well as specific capacity 942 mAh g$^{-1}$ at 5.0 A g$^{-1}$. This facile interfacial engineering strategy by the construction of MIECI in situ derived from fluoride compounds can be extended to other alloy-type anode materials and has large commercial potential for Li-ion batteries.

## 4. Experimental Section

*Fabrication of MgF$_2$-Coated p-Si*: The Si/Mg$_3$N$_2$ composites were prepared by nitridation of magnesium silicide (Mg$_2$Si) with a size of 1 µm at 750 °C for 3 h[4,29] and 1 g of the Si/Mg$_3$N$_2$ composite was dispersed in 100 mL of HCl (1 M) and stirred continuously in a water bath at 60 °C for 3 h. 0.5 M NH$_4$F was then added dropwise and after stirring for 3 h, F$^-$ and Mg$^{2+}$ in the solution reacted to form MgF$_2$ precipitate that adsorbed on the porous Si skeleton. The amounts of the NH$_4$F were 0, 0.2, 0.4, and 1.0 mL. The suspensions were washed with an adequate amount of absolute ethanol and deionized water and the products were freeze-dried and then heated at a rate of 2 °C min$^{-1}$ to 400 °C for 5 h in a horizontal tube furnace under argon (Ar). The samples with different concentrations of MgF$_2$ were labeled as p-Si, p-Si@MgF$_2$, p-Si@MgF$_2$-1, and p-Si@MgF$_2$-2, respectively.

*Materials Characterization*: The elemental concentrations were determined by inductively-coupled plasma optical emission spectrometer (ICP-OES, ICAP7400) after HF and HNO$_3$ etching. The micromorphology was observed by field-emission scanning electron microscopy (FE-SEM, Apreo S HiVac), and the fine structure and chemical composition on the nanoscale were determined by field-emission transmission electron microscopy (FE-TEM, JEM-200), scanning TEM (STEM), and energy-dispersive X-ray spectroscopy (EDS, Aztec Ultim Live 100 X). The porosity information of samples was obtained from nitrogen adsorption isotherm measurement by Brunauer-Emmett-Teller (BET, Autosorb- iQ-MP/XR). The phases and in situ electrochemical lithiation were characterized on the Bruker X-ray diffractometer (XRD, SmartLab SE) using Cu K$_\alpha$

radiation ($\lambda$ = 0.15406 nm) in the 2 $\theta$ range from 10° to 90°. In situ Raman scattering was performed on the Horiba (HR revolution) at an excitation wavelength of 532 nm and *operando* Fourier Transform Infrared spectroscopy (FTIR, Nicolet 460) was carried out on the electrolytic cells (Beijing Science Star Technology). To observe the morphology and composition of p-Si@MgF$_2$ and p-Si after cycling, the electrodes disassembled from the cells were rinsed with excess dimethyl carbonate (DMC) solution in an Ar-filled glove box. The surface composition of the electrodes in different states after cleaning was characterized by X-ray photoelectron spectroscopy (XPS, AXIS SUPRA+). Negative-mode time of flight secondary ion mass spectrometry (ToF-SIMS, ION-TOF GmbH) was used to determine the chemical composition in the electrodes. The Bi$_1^+$ ion beam (30 keV) was used to sputter an area of 81 × 81 µm$^2$ surface and a Cs$^+$ ion beam (1 KeV) was used for a 200 × 200 µm$^2$ area. The elasticity modulus and micromorphology of the electrodes after cycling were determined by atomic force microscopy (AFM, Dimension ICON).

*Electrochemical Characterization*: *Half cell*: The p-Si@MgF$_2$, p-Si@ MgF$_2$-1, p-Si@MgF$_2$-2, and p-Si electrodes were prepared by mixing the active materials, carbon black (Super C65), and polyacrylic acid solution (PAA, 4 wt.%) with a mass ratio of 70: 10: 20 to form a slurry. The slurry was cast on a copper foil with a mass loading of 0.8–1.2 mg cm$^{-2}$. After vacuum drying at 80 °C for 24 h and cutting into circular samples with a diameter of 12 mm, the electrodes were calendared to increase the electrode density. The coin-type 2032 half cells were assembled in an Ar-filled glove box (Vigor SG1200/750TS-C) with the counter electrode being a pure Li foil and the separator being a Celgard 2400 film. The electrolyte was prepared by dissolving LiPF$_6$ (1 M) and fluoroethylene carbonate (FEC) (10 vol.%) in a solution of ethylene carbonate (EC) and diethyl carbonate (DEC) with a volume ratio of 1:1. An electrochemical workstation (VSP 300, Bio-Logics Co. Ltd.) was employed for cyclic voltammetry (CV) and electrochemical impedance spectroscopy (EIS). The cycling and rate characteristics of the half-cells were evaluated using a battery tester (LAND CT2001A, Wuhan Land Electronics Co. Ltd.) in the potential range between 0.01 and 1.0 V (vs. Li/Li$^+$) at a current density of 0.1 A g$^{-1}$ for the initial three cycles and 1.0 A g$^{-1}$ for the subsequent cycles.

*Full-cell*: First, the active materials (LFP, 90 wt.%), carbon black (C60, 5 wt.%), and polyvinylidene fluoride (PVDF, 5 wt.%) were mixed with *N*-methyl-2-pyrrolidinone(NMP) solution to form a slurry. The homogeneous slurry was cast on the Al foil and dried at 100 °C for 12 h. Then, the prepared cathodes were cut into disks with a diameter of 10 mm with an areal capacity of ≈1.25 mAh cm$^{-2}$. The p-Si/Graphite and p-Si@ MgF$_2$/Graphite anodes were prepared in a similar method. The active materials (p-Si or p-Si@MgF$_2$ 10 wt.%, Graphite 90 wt.%, 650 mAh g$^{-1}$) 80%, carbon black (C60) 10 wt.%, carboxymethyl cellulose (CMC) 5 wt.% and styrene butadiene rubber (SBR) 5 wt.% were mixed with distilled water to form a slurry. The homogeneous slurry was cast on the Cu foil and dried at 80 °C for 12 h. Then, the dried anodes were cut into disks with a diameter of 12 mm. Before assembling into a full cell, the p-Si/ Graphite and p-Si@MgF$_2$/Graphite anodes were prelithiated in the half cell with Li foil activated at 0.1 A g$^{-1}$ for 3 cycles. Then, the full cells were assembled into the CR2032 cells with the prelithiated p-Si/Graphite and p-Si@MgF$_2$/Graphite anodes and LFP cathodes, which had a similar areal capacity of ≈1.17 mAh cm$^{-2}$. For p-Si or p-Si@MgF$_2$/Graphite|LFP full cells, cut-off voltages were 2.5–3.7 V (1 C = 170 mAh g$^{-1}$).

## Supporting Information

Supporting Information is available from the Wiley Online Library or from the author.

## Acknowledgements

## Conflict of Interest

The authors declare no conflict of interest.

## Data Availability Statement

The data that support the findings of this study are available in the supplementary material of this article.

## Keywords

[1] S. Park, S. Y. Jeong, T. K. Lee, M. W. Park, H. Y. Lim, J. Sung, J. Cho, S. K. Kwak, S. Y. Hong, N.-S. Choi, *Nat. Commun.* **2021**, *12*, 838.

[2] B. Xiang, W. L. An, J. J. Fu, S. X. Mei, S. G. Guo, X. M. Zhang, B. Gao, P. K. Chu, *Rare Met.* **2021**, *40*, 383.

[3] Y. L. An, Y. Tian, H. Wei, B. J. Xi, S. L. Xiong, J. K. Feng, Y. T. Qian, *Adv. Funct. Mater.* **2020**, *30*, 1908721.

[4] S. X. Mei, S. G. Guo, B. Xiang, J. G. Deng, J. J. Fu, X. M. Zhang, Y. Zheng, B. Gao, P. K. Chu, K. F. Huo, *J. Energy Chem.* **2022**, *69*, 616.

[5] Y. Ren, X. C. Yin, R. Xiao, T. S. Mu, H. Huo, P. J. Zuo, Y. L. Ma, X. Q. Cheng, Y. Z. Gao, G. P. Yin, Y. Li, C. Y. Du, *Chem. Eng. J.* **2022**, *43*, 133982.

[6] X. Sun, Y. Y. Wang, Y. M. Zhang, L. R. Hou, C. Z. Yuan, *Adv. Energy Sustain. Res.* **2022**, *3*, 2200028.

[7] J. D. McBrayer, M.-T. F. Rodrigues, M. C. Schulze, D. P. Abraham, C. A. Apblett, I. Bloom, G. M. Carroll, A. M. Colclasure, C. Fang, K. L. Harrison, G. Liu, S. D. Minteer, N. R. Neale, G. M. Veith, C. S. Johnson, J. T. Vaughey, A. K. Burrell, B. Cunningham, *Nat. Energy* **2021**, *6*, 866.

[8] S. Bazlen, P. Heugel, O. von Kessel, W. Commerell, J. Tübke, *J. Energy Storage* **2022**, *49*, 104044.

[9] Z. W. Zhang, Y. Z. Li, R. Xu, W. J. Zhou, Y. B. Li, S. T. Oyakhire, Y. C. Wu, J. W. Xu, H. S. Wang, Z. A. Yu, D. T. Boyle, W. Huang, Y. S. Ye, H. Chen, J. Y. Wan, Z. N. Bao, W. Chiu, Y. Cui, *Science* **2022**, *375*, 66.

[10] A. P. Wang, S. Kadam, H. Li, S. Q. Shi, Y. Qi, *npj Comput. Mater.* **2018**, *4*, 15.

[11] Z. Cao, X. Y. Zheng, Q. T. Qu, Y. H. Huang, H. H. Zheng, *Adv. Mater.* **2021**, *33*, 2103178.

[12] C. Stetson, T. Yoon, J. Coyle, W. Nemeth, M. Young, A. Norman, S. Pylypenko, C. Ban, C.-S. Jiang, M. Al-Jassim, A. Burrell, *Nano Energy* **2019**, *55*, 477.

[13] X. Y. Shan, Y. Zhong, L. J. Zhang, Y. Q. Zhang, X. H. Xia, X. L. Wang, J. P. Tu, *J. Phys.Chem. C* **2021**, *125*, 19060.

[14] Y. Z. Li, W. Huang, Y. B. Li, A. Pei, D. T. Boyle, Y. Cui, *Joule* **2018**, *2*, 2167.

[15] H. L. Dai, J. Dong, M. J. Wu, Q. M. Hu, D. N. Wang, L. Zuin, N. Chen, C. Lai, G. X. Zhang, S. H. Sun, *Angew. Chem., Int. Ed.* **2021**, *60*, 19852.

[16] Q. Y. Wang, M. Zhu, G. R. Chen, N. Dudko, Y. Li, H. J. Liu, L. Y. Shi, G. Wu, D. S. Zhang, *Adv. Mater.* **2022**, *34*, 2109658.

[17] L. Sun, Y. X. Liu, R. Shao, J. Wu, R. Y. Jiang, Z. Jin, *Energy Storage Mater.* **2022**, *46*, 482.

[18] Z. Cao, X. Y. Zheng, Y. Wang, W. B. Huang, Y. C. Li, Y. H. Huang, H. H. Zheng, *Nano Energy* **2022**, *93*, 106811.

[19] H. Z. Wang, H. Man, J. H. Yang, J. H. Zang, R. C. Che, F. Wang, D. L. Sun, F. Fang, *Adv. Funct. Mater.* **2022**, *32*, 2109887.

[20] V. Etacheri, O. Haik, Y. Goffer, G. A. Roberts, I. C. Stefan, R. Fasching, D. Aurbach, *Langmuir* **2012**, *28*, 965.

[21] D. Aurbach, K. Gamolsky, B. Markovsky, Y. Gofer, M. Schmidt, U. Heider, *Electrochim. Acta* **2002**, *47*, 1423.

[22] J.-B. Fang, S.-Z. Chang, Q. Ren, T.-Q. Zi, D. Wu, A.-D. Li, *ACS Appl. Mater. Interfaces* **2021**, *13*, 32520.

[23] J. Chen, X. L. Fan, Q. Li, H. B. Yang, M. R. Khoshi, Y. B. Xu, S. Hwang, L. Chen, X. Ji, C. Y. Yang, H. X. He, C. M. Wang, E. Garfunkel, D. Su, O. Borodin, C. S. Wang, *Nat. Energy* **2020**, *5*, 386.

[24] J. Salonen, V.-P. Lehto, *Chem. Eng. J.* **2008**, *137*, 162.

[25] J. Wang, Z. Yang, B. G. Mao, Y. X. Wang, Y. Jiang, M. H. Cao, *ACS Energy Lett.* **2022**, *7*, 2781.

[26] Q. Ai, D. P. Li, J. G. Guo, G. M. Hou, Q. Sun, Q. D. Sun, X. Y. Xu, W. Zhai, L. Zhang, J. K. Feng, P. C. Si, J. Lou, L. J. Ci, *Adv. Mater. Inter.* **2019**, *6*, 1901187.

[27] T. X. Kang, J. H. Tan, X. C. Li, J. L. Liang, H. Wang, D. Shen, Y. Wu, Z. M. Huang, Y. Lu, Z. Q. Tong, C.-S. Lee, *J. Mater. Chem. A* **2021**, *9*, 7807.

[28] J. Lin, H. Peng, J.-H. Kim, B. R. Wygant, M. L. Meyerson, R. Rodriguez, Y. Liu, K. Kawashima, D. Gu, D.-L. Peng, H. Guo, A. Heller, C. B. Mullins, *ACS Appl. Mater. Interfaces* **2020**, *12*, 18465.

[29] W. L. An, B. Gao, S. X. Mei, B. Xiang, J. J. Fu, L. Wang, Q. B. Zhang, P. K. Chu, K. F. Huo, *Nat. Commu.* **2019**, *10*, 1447.

[30] S. X. Mei, Y. F. Liu, J. J. Fu, S. G. Guo, J. G. Deng, X. Peng, X. M. Zhang, B. Gao, K. F. Huo, P. K. Chu, *Appl. Surf. Sci.* **2021**, *563*, 150280.

[31] Q. S. Xu, X. F. Yang, M. M. Rao, D. C. Lin, K. Yan, R. A. Du, J. T. Xu, Y. G. Zhang, D. Q. Ye, S. H. Yang, G. M. Zhou, Y. Y. Lu, Y. C. Qiu, *Energy Storage Mater.* **2020**, *26*, 73.

[32] S.-Q. Li, L. Zhang, T.-T. Liu, Y.-W. Zhang, C. Guo, Y. Wang, F.-H. Du, *Adv. Mater.* **2022**, *34*, 2201801.

[33] L. W. Tan, C. L. Wei, Y. C. Zhang, Y. L. An, S. L. Xiong, J. K. Feng, *Chem. Eng. J.* **2022**, *442*, 136243.

[34] J. L. Jiang, X. F. Hu, S. Y. Lu, C. Shen, S. S. Huang, X. Y. Liu, Y. Jiang, J. J. Zhang, B. Zhao, *Energy Storage Mater.* **2023**, *54*, 885.

[35] C. P. Yang, H. Xie, W. W. Ping, K. Fu, B. Y. Liu, J. C. Rao, J. Q. Dai, C. W. Wang, G. Pastel, L. B. Hu, *Adv. Mater.* **2019**, *31*, 1804815.

[36] J. F. Yang, N. Solomatin, A. Kraytsberg, Y. Ein-Eli, *ChemistrySelect* **2016**, *1*, 572.

[37] X. S. Wang, S. W. Wang, H. R. Wang, W. Q. Tu, Y. Zhao, S. Li, Q. Liu, J. R. Wu, Y. Z. Fu, C. P. Han, F. Y. Kang, B. H. Li, *Adv. Mater.* **2021**, *33*, 2007945.

[38] Z. K. Ma, J. W. Chen, J. Vatamanu, O. Borodin, D. Bedrov, X. G. Zhou, W. G. Zhang, W. S. Li, K. Xu, L. D. Xing, *Energy Storage Mater.* **2022**, *45*, 903.

[39] C. P. Lv, C. F. Lin, X. S. Zhao, *Adv. Energy Mater.* **2022**, *12*, 2102550.

[40] R. F. H. Hernandha, P. C. Rath, B. Umesh, J. Patra, C.-Y. Huang, W.-W. Wu, Q.-F. Dong, J. Li, J.-K. Chang, *Adv. Funct. Mater.* **2021**, *31*, 2104135.

[41] B. H. Han, C. Liao, F. Dogan, S. E. Trask, S. H. Lapidus, J. T. Vaughey, B. Key, *ACS Appl. Mater. Interfaces* **2019**, *11*, 29780.

[42] X. Li, J. A. Gilbert, S. E. Trask, R. Uppuluri, S. H. Lapidus, S. Cora, N. Sa, Z. Z. Yang, I. D. Bloom, F. Dogan, J. T. Vaughey, B. Key, *Chem. Mater.* **2021**, *33*, 4960.

# Design and Electrochemical Mechanism of the MgF₂ Coating as a Highly Stable and Conductive Interlayer on the Si Anode for High-Performance Li-Ion Batteries

*Shixiong Mei, Ben Xiang, Siguang Guo, Jiaguo Deng, Jijiang Fu, Xuming Zhang, Yang Zheng, Biao Gao,\* Kaifu Huo,\* and Paul K Chu*

# Supporting Information

**Design and Electrochemical Mechanism of the MgF₂ Coating as a Highly Stable and Conductive Interlayer on the Si Anode for High-Performance Li-Ion Batteries**

Shixiong Mei[a,b,1], Ben Xiang[a,b,1], Siguang Guo[a], Jiaguo Deng[a], Jijiang Fu[a], Xuming Zhang[a], Yang Zheng[a], Biao Gao[a,*], Kaifu Huo[b,*], Paul K Chu[c]

[a] *The State Key Laboratory of Refractories and Metallurgy and Institute of Advanced Materials and Nanotechnology, Wuhan University of Science and Technology, Wuhan 430081, China*

[b] *Wuhan National Laboratory for Optoelectronics (WNLO), School of Optical and Electronic Information Huazhong University of Science and Technology Wuhan 430074, China*

[c] *Department of Physics, Department of Materials Science & Engineering, and Department of Biomedical Engineering, City University of Hong Kong, Tat Chee Avenue, Kowloon, Hong Kong, China*

\* Corresponding authors: gaobiao@wust.edu.cn (B. Gao); kfhuo@hust.edu.cn (K.F. Huo)

[1] These authors contributed equally to the work

**Supporting Figures**
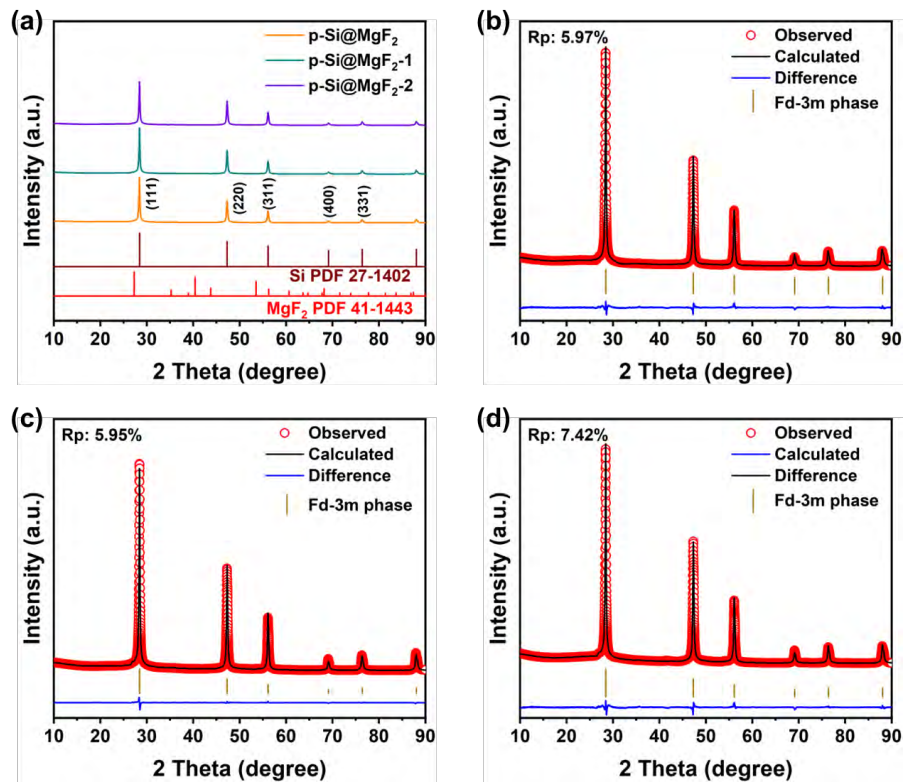
**Figure S1.** (a) The XRD patterns of p-Si@MgF$_2$, p-Si@MgF$_2$-1, and p-Si@MgF$_2$-2. Rietveld refinements from XRD patterns of (b) p-Si@MgF$_2$, (c) p-Si@MgF$_2$-1, and (d) p-Si@MgF$_2$-2.
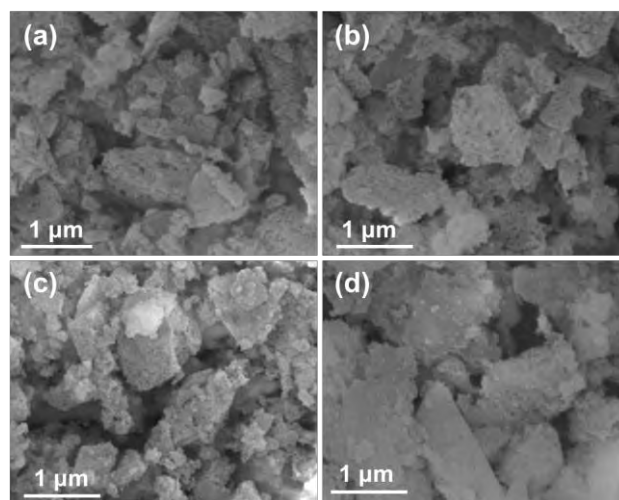


**Figure S2.** SEM images of (a) p-Si, (b) p-Si@MgF$_2$, (c) p-Si@MgF$_2$-1, and (d) p-Si@MgF$_2$-2.
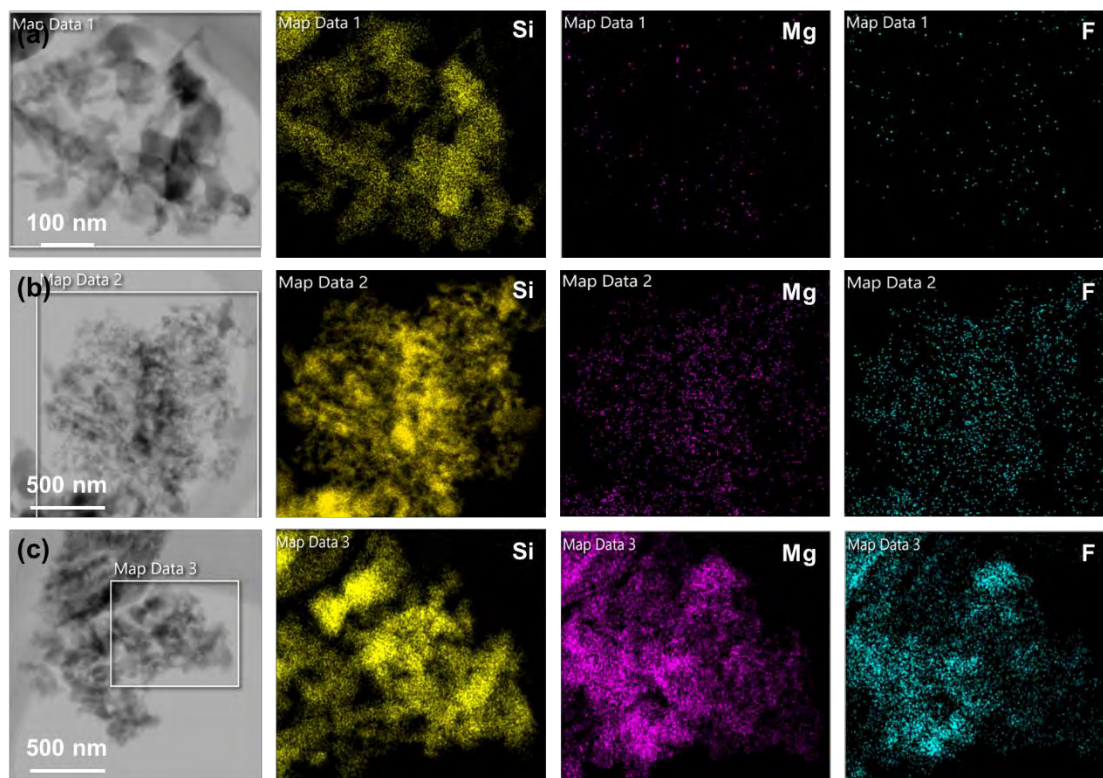
**Figure S3.** STEM images and corresponding EDS maps of Si, Mg, and N: (a) p-Si@MgF$_2$, (b) p-Si@MgF$_2$-1, and (c) p-Si@MgF$_2$-2.
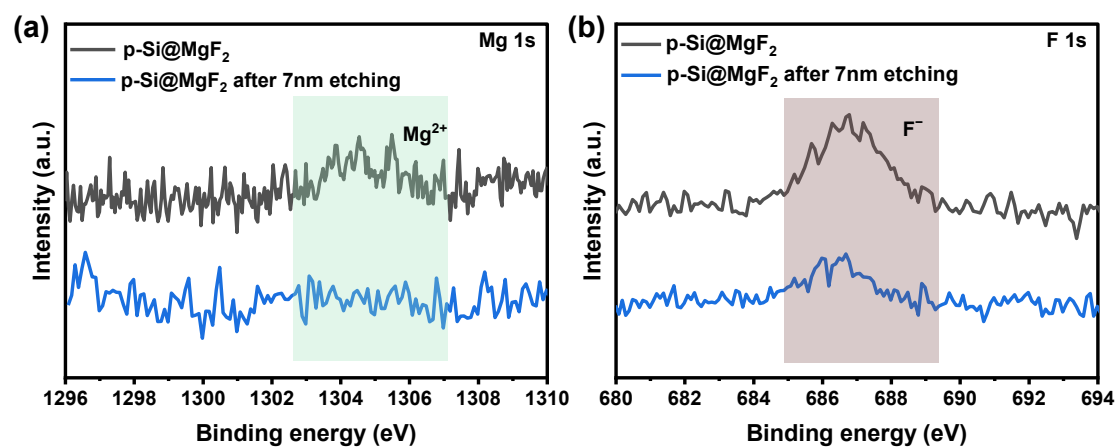


**Figure S4.** High-resolution XPS spectra of (a) Mg 1$s$ and (b) F 1$s$ of p-Si@MgF$_2$ before and after Ar ion etching.
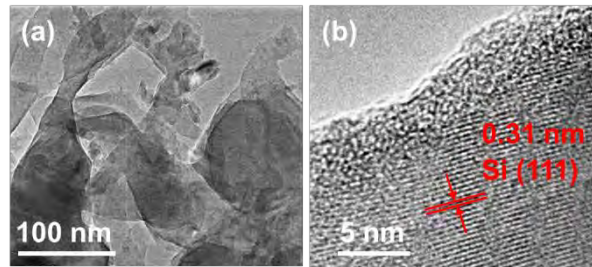
**Figure S5.** (a) TEM and (b) HR-TEM images of p-Si.
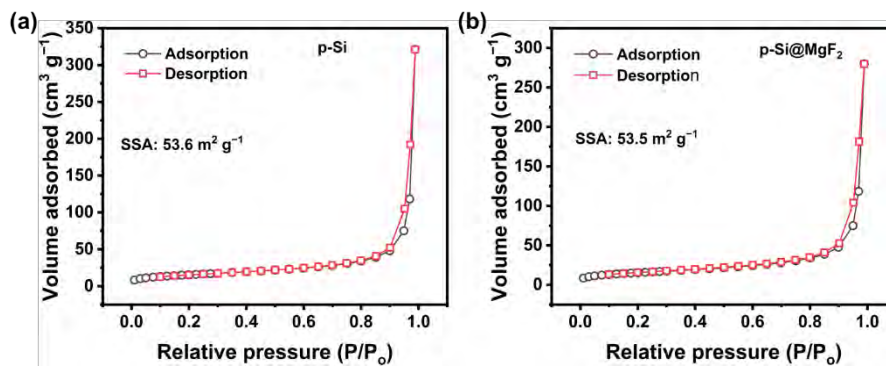


**Figure S6.** Nitrogen adsorption/desorption isotherms of p-Si (a) and p-Si@MgF$_2$.
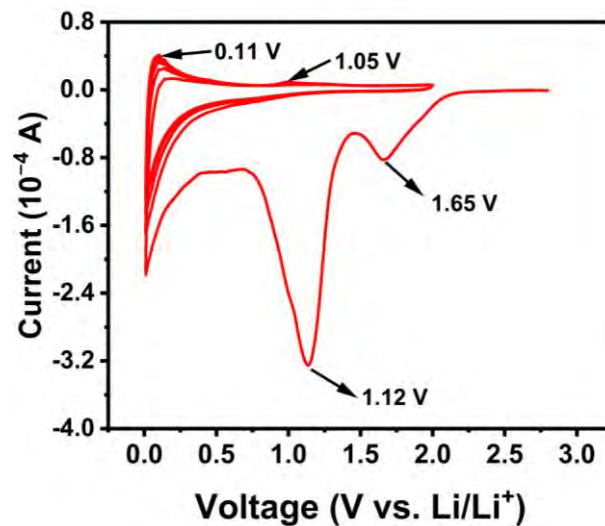


**Figure S7.** CV curves of pure MgF$_2$ electrode at 0.1 mV s$^{-1}$.

**In-situ XRD cell**

**X-ray**

Beryllium plate
Sample on the Cu mesh
Separator
Li foil

**In-situ FTIR cell**

**Infrared (IR) detector**

Diamond optical window
Sample on the Cu mesh
Separator
Li foil

**In-situ Raman cell**

**Raman laser light**

Glass plate
Sample on the Cu mesh
Separator
Li foil
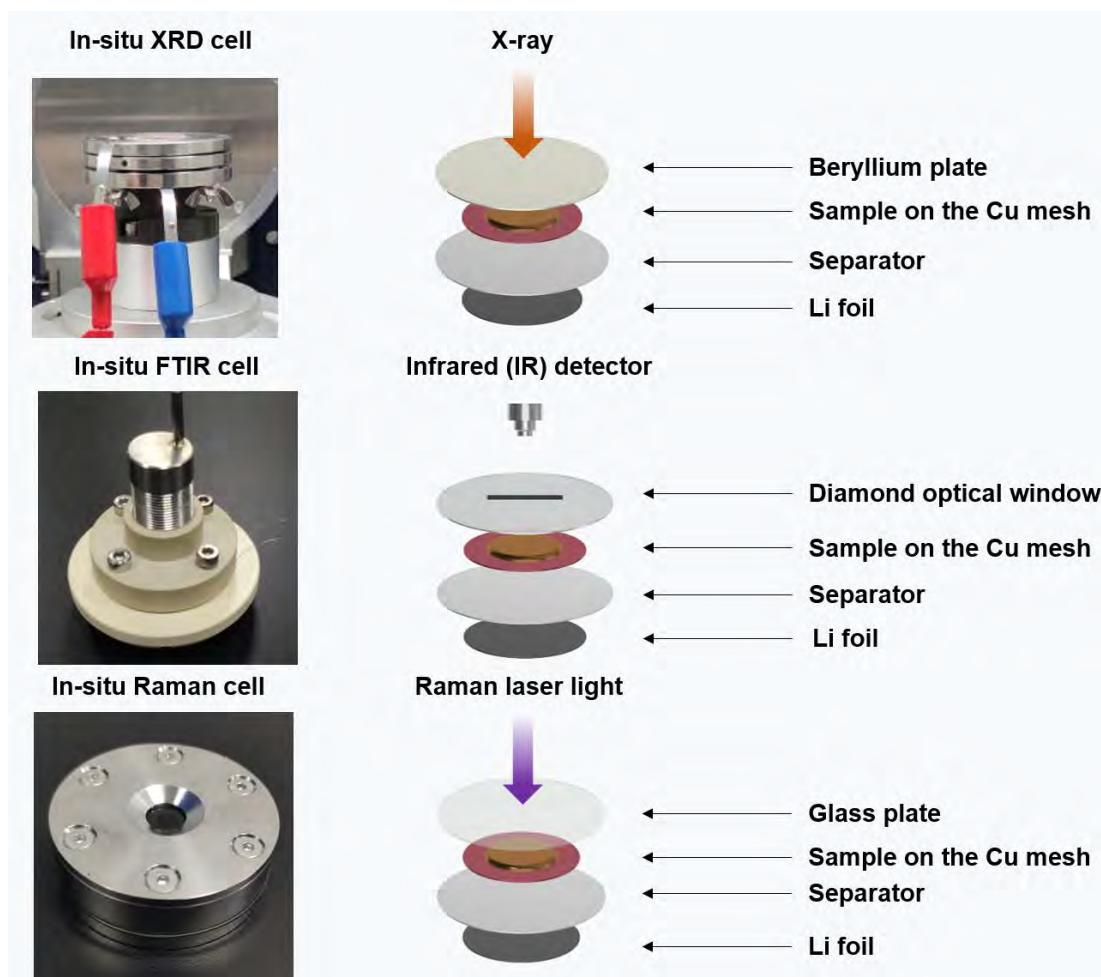
**Figure S8**. Pictures and schematic diagrams of the internal structure of the *in situ* cells.
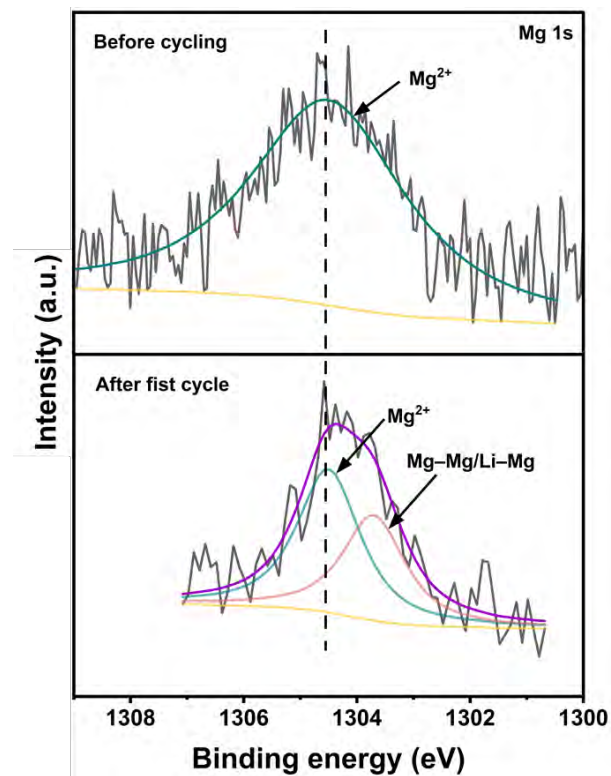
**Figure S9.** High-resolution XPS spectra of Mg 1*s* of the p-Si@MgF$_2$-2 anode after first cycle.
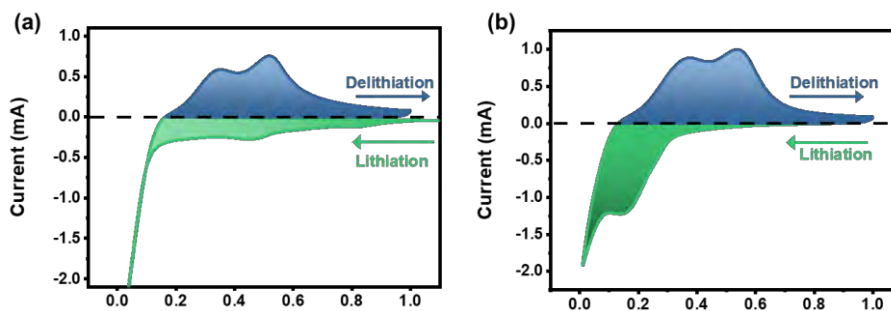


**Figure S10.** CV curves acquired at 0.1 mV s$^{-1}$: (a) p-Si and (b) p-Si@MgF$_2$ anodes.
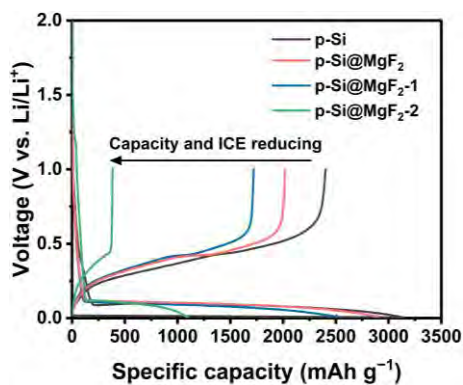
**Figure S11.** Initial charging and discharging curves p-Si, p-Si@MgF$_2$, p-Si@MgF$_2$-1 and p-Si@MgF$_2$-2 at 0.1 A g$^{-1}$ at 0.1 A g$^{-1}$, respectively.
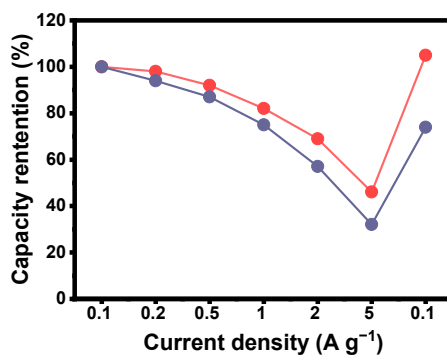


**Figure S12.** Capacity retention of the p-Si@MgF$_2$ and p-Si anodes after the rate test.
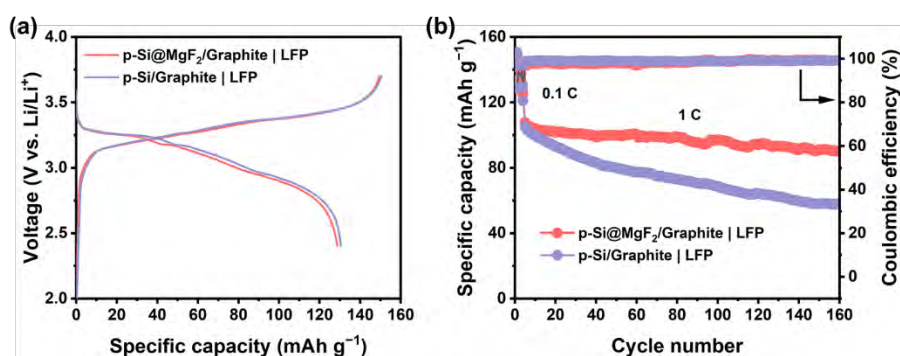


**Figure S13.** (a) Initial charging and discharging curves at 0.1 C of p-Si@MgF$_2$/Graphite | LFP and p-Si/Graphite | LFP full cells (1 C = 170 mAh g$^{-1}$). (b) Cycling performance of at 1 C after activating 3 cycles at 0.1 C.
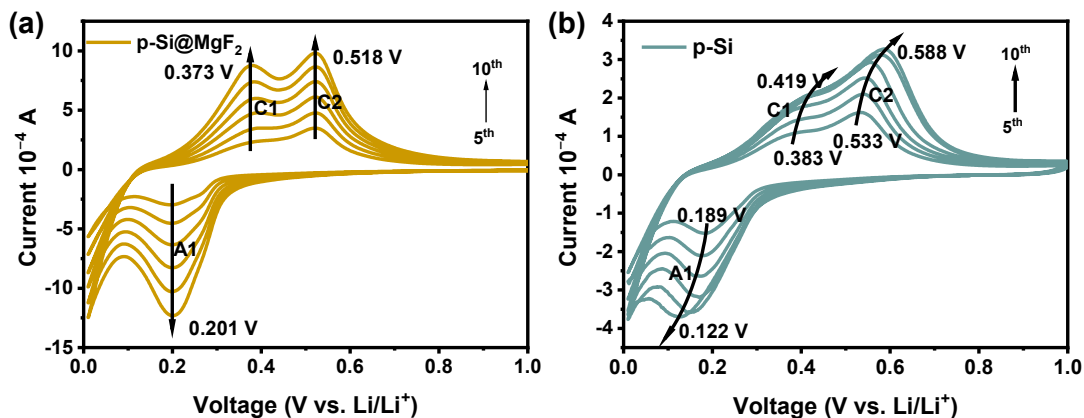
**Figure S14.** CV curves of (a) p-Si@MgF$_2$ and (b) p-Si at 0.1 mV s$^{-1}$ from 5$^{th}$ to 10$^{th}$ cycles.



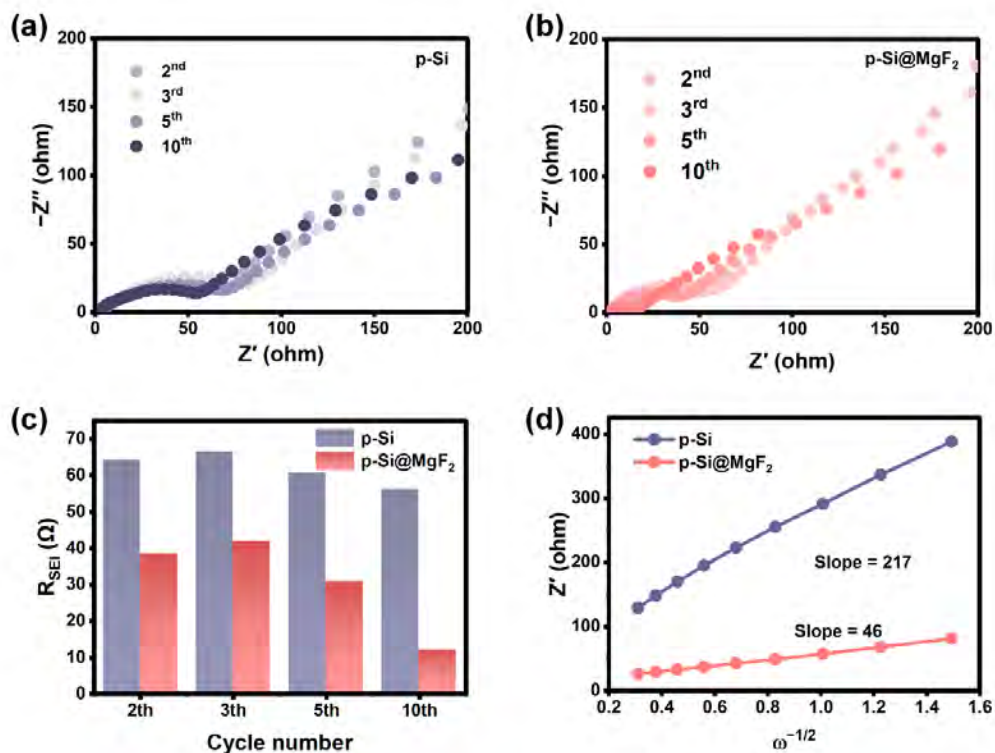**Fig. 15.** EIS profiles of (a) p-Si and (b) p-Si@MgF$_2$ anodes after different cycles at 0.1 A g$^{-1}$; (c) Comparison of R$_{SEI}$ of the p-Si and p-Si@MgF$_2$ anodes; (d) Z′ versus ω$^{-1/2}$ plots of the p-Si and p-Si@MgF$_2$ anodes after 10 cycles.
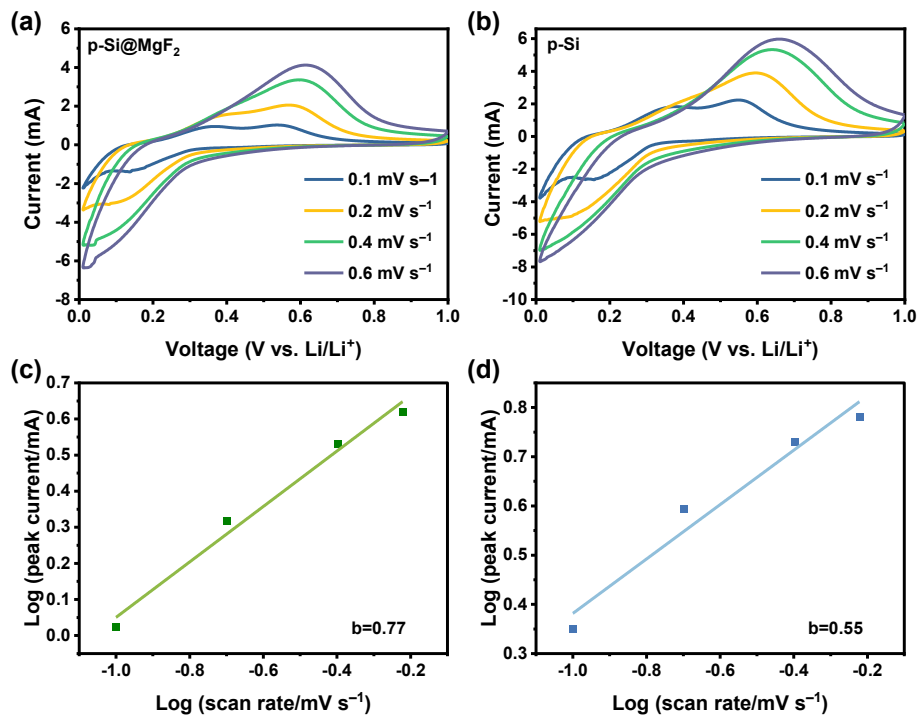
**Figure S16.** CV curves of (a) p-Si@MgF$_2$ and (b) p-Si acquired at different scanning rates; Relationship between scanning rates and peak currents of (c) p-Si@MgF$_2$ and (d) p-Si.
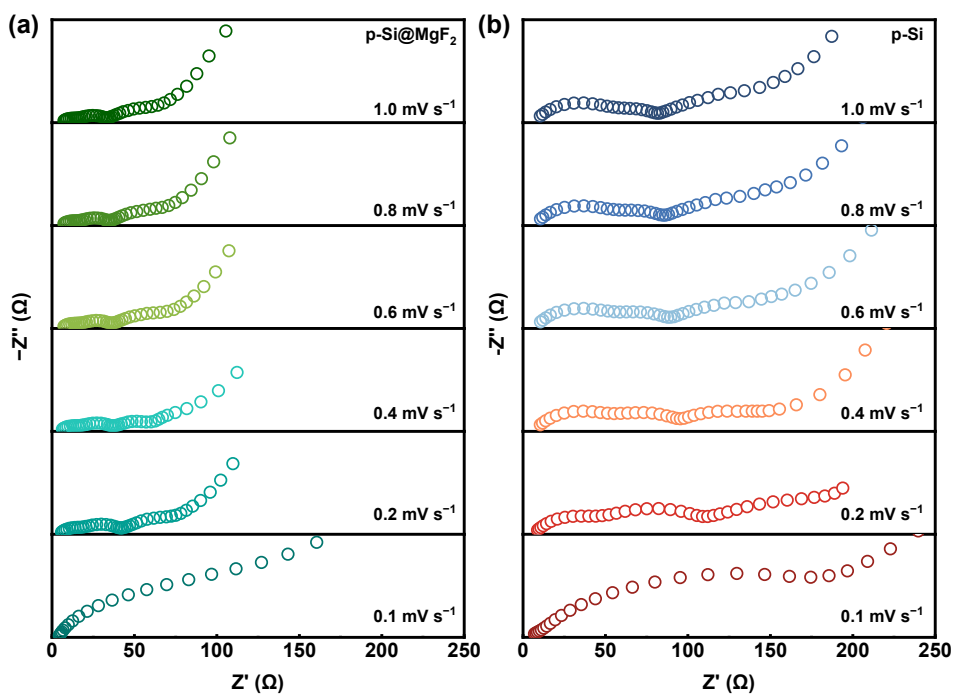


**Figure S17.** EIS profiles of (a) p-Si@MgF$_2$ and (b) p-Si at different scanning rates.
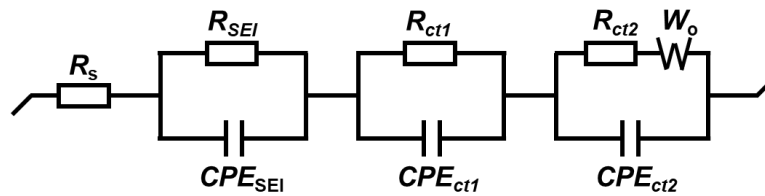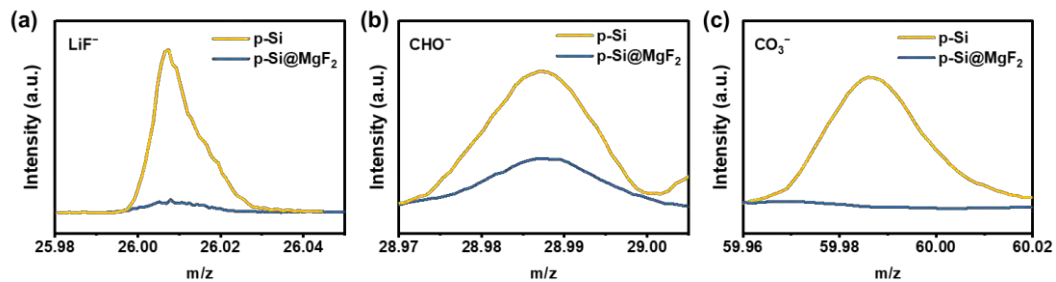
**Figure S18.** Corresponding equivalent circuit.



**Figure S19.** ToF-SIMS spectra of the secondary ion fragments of the p-Si and the p-Si@MgF$_2$ anodes after 10 cycles: (a) LiF$^-$, (b) CHO$^-$, and (c) CO$_3^-$.
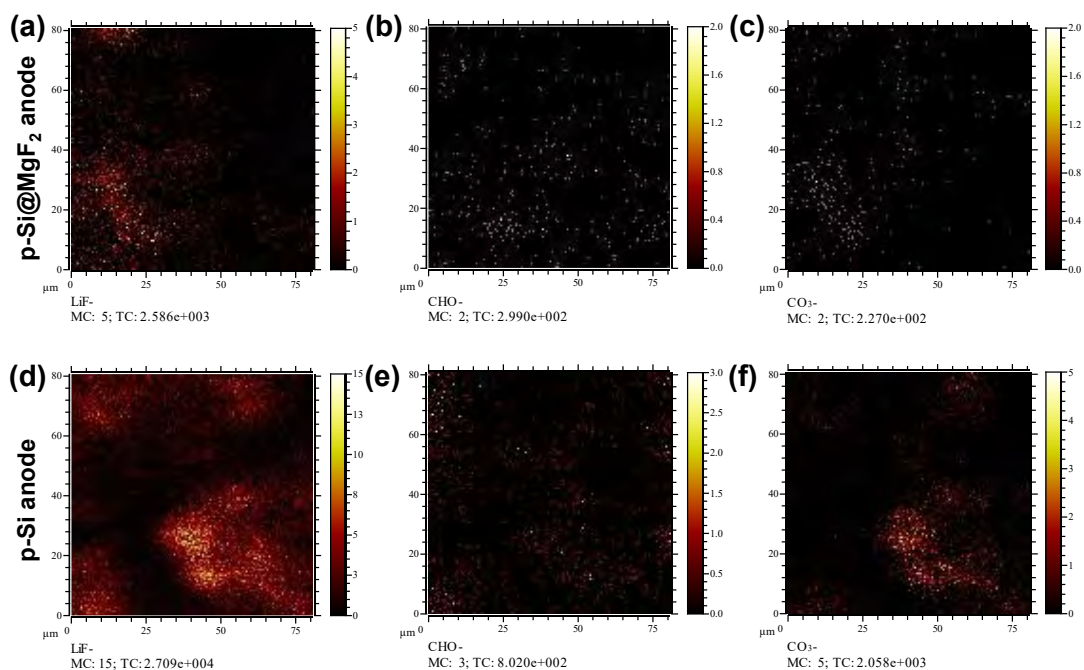


**Figure S20.** TOF-SIMS maps in the negative mode: (a, d) LiF$^-$, (b, e) CHO$^-$, and (c, f) CO$_3^-$ of p-Si@MgF$_2$ and p-Si.

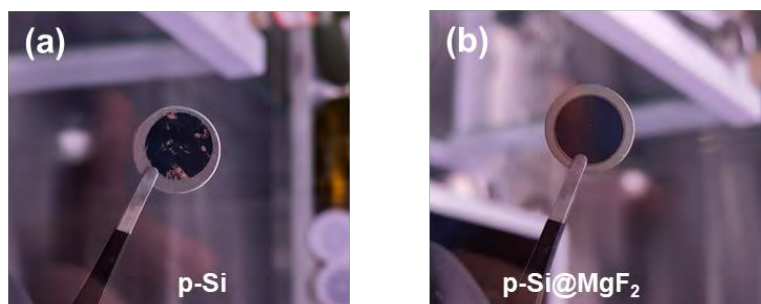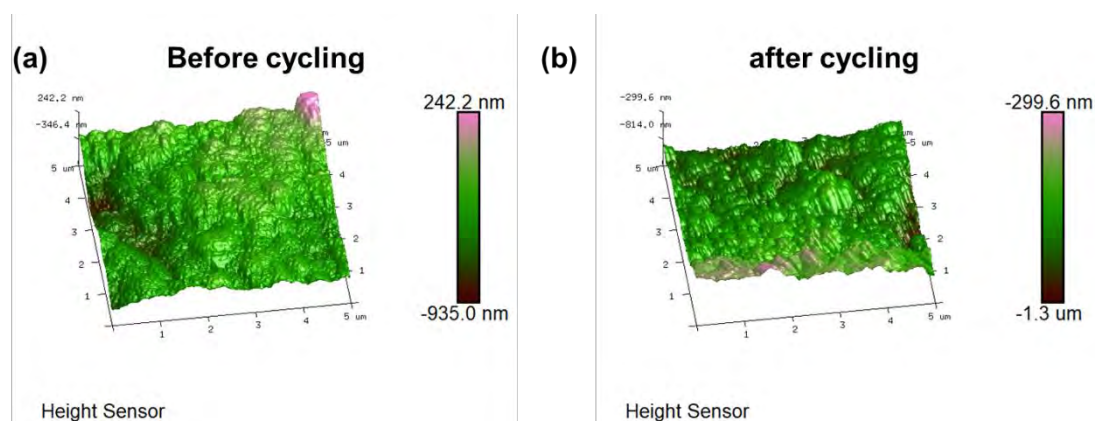**Figure S21.** Photographs of (a) p-Si and (b) p-Si@MgF$_2$ anodes after cycling.



**Figure S22.** AFM surface morphologies of the p-Si@MgF$_2$ electrode ($5 \times 5$ μm$^2$) before and after cycling.

**Table S1.** Mg concentration (%) in p-Si@MgF$_2$, p-Si@MgF$_2$-1, and p-Si@MgF$_2$-2 determined by ICP-OES.

| Samples | Mg (%) |
|---|---|
| p-Si@MgF$_2$ | 0.22% |
| p-Si@MgF$_2$-1 | 0.62% |
| p-Si@MgF$_2$-2 | 1.87% |

**Table S2.** Comparison of electrochemical performance in this work to those of reported Si-based anode materials.

| Materials | Rate performance | Cyclic stability | Refs. |
|---|---|---|---|
| p-Si@MgF$_2$ | 942 mAh g$^{-1}$ at 5 A g$^{-1}$ | 1600 mAh g$^{-1}$ at 1 A g$^{-1}$ after 200 cycles | **This work** |
| PFe-Si@NCNS | 491 mAh g$^{-1}$ at 5 A g$^{-1}$ | 992 mAh g$^{-1}$ at 0.5 A g$^{-1}$ after 100 cycles | [1] |
| PCSi-2 | 1118 mAh g$^{-1}$ at 6.6 A g$^{-1}$ | 1130 mAh g$^{-1}$ at 1 A g$^{-1}$ after 500 cycles | [2] |
| SiNPs-TMSPA-LCP | 942 mAh g$^{-1}$ at 5 A g$^{-1}$ | 1000 mAh g$^{-1}$ at 1 A g$^{-1}$ after 300 cycles | [3] |
| Si@25-PU | 1420 mAh g$^{-1}$ at 5 A g$^{-1}$ | 865 mAh g$^{-1}$ at 1 A g$^{-1}$ after 350 cycles | [4] |
| Si@SiO$_x$@C–NB | 690 mAh g$^{-1}$ at 5 A g$^{-1}$ | 1300 mAh g$^{-1}$ at 0.5 A g$^{-1}$ after 340 cycles | [5] |
| Si/Ag/C | 1113 mAh g$^{-1}$ at 2 A g$^{-1}$ | 1093 mAh g$^{-1}$ at 1 A g$^{-1}$ after 300 cycles | [6] |
| H–SiNS/C | 820 mAh g$^{-1}$ at 4 A g$^{-1}$ | 830 mAh g$^{-1}$ at 2 A g$^{-1}$ after 500 cycles | [7] |
| p-Si@C | 885 mAh g$^{-1}$ at 6 A g$^{-1}$ | 1563 mAh g$^{-1}$ at 0.1 A g$^{-1}$ after 100 cycles | [8] |
| PCC-nSi-2 | 1139 mAh g$^{-1}$ at 2 A g$^{-1}$ | 1406 mAh g$^{-1}$ at 0.6 A g$^{-1}$ after 400 cycles | [9] |
| Si@MoSe$_2$ | ~500 mAh g$^{-1}$ at 5 A g$^{-1}$ | 1120 mAh g$^{-1}$ at 0.2 A g$^{-1}$ after 100 cycles | [10] |

**Table S3.** $R_{ct}$ and $R_{SEI}$ of the p-Si and Si@MgF$_2$ electrodes after cycling at different scanning rates.

| Rates | p-Si | | | | p-Si@MgF$_2$ | | | |
|---|---|---|---|---|---|---|---|---|
| | $R_s$ ($\Omega$) | $R_{SEI}$ ($\Omega$) | | | $R_s$ ($\Omega$) | $R_{SEI}$ ($\Omega$) | $R_{ct1}$ ($\Omega$) | $R_{ct2}$ ($\Omega$) |
| 0.1 | 4.739 | 253.9 | - | - | 3.653 | 29 | 61.79 | - |
| 0.2 | 7.106 | 40.94 | 58.5 | 66.81 | 4.904 | 13.77 | 22.97 | 36.93 |
| 0.4 | 7.256 | 49.71 | 28.78 | 91.12 | 5.221 | 11.58 | 18.84 | 10.22 |
| 0.6 | 7.406 | 49.65 | 28.26 | 99.64 | 6.086 | 10.88 | 17.32 | 29 |
| 0.8 | 7.46 | 49.62 | 24.34 | 120.4 | 6.039 | 9.907 | 16.62 | 24.96 |
| 1.0 | 7.358 | 49.82 | 19.85 | 143.5 | 6.135 | 9.47 | 15.43 | 22.54 |

**Supporting References**

[1] Y. J. Li, P. Xiao, J. Z. Xiong, J. Luo, P. Zhou, X. L. Xie, Y. Li, M. L. Chen, *J. Alloys Compd.* **2023**, *945*, 169331.

[2] Q. Y. Wang, M. Zhu, G. R. Chen, N. Dudko, Y. Li, H. J. Liu, Shi, L.; G. Wu, D. S. Zhang, *Adv. Mater.* **2022**, *34*, 2109658.

[3] S. Y. Pan, J. W. Han, Y. Q. Wang, Z. S. Li, F. Q. Chen, Y. Guo, Z. S. Han, K. F. Xiao, Z. C. Yu, M. Y. Yu, S. C. Wu, D. -W. Wang, Q. -H. Yang, *Adv. Mater.* **2022**, *34*, 2203617.

[4] T. S. Mu, Y. P. Sun, C. H. Wang, Y. Zhao, K. Doyle-Davis, J. N. Liang, X. L. Sui, R. Y. Li, C. Y. Du, P. J. Zuo, G. P. Yin, X. L. Sun, *Nano Energy* **2022**, *103*, 107829.

[5] J. Zhou, Y. Lu, L. S. Yang, W. Q. Zhu, W. F. Liu, Y. H. Yang, K. Y. Liu, *Carbon Energy* **2022**, *4*, 399.

[6] Z. Zhang, F. Xi, Q. Ma, X. Wan, S. Li, W. Ma, X. Chen, Z. Chen, R. Deng, J. Ji, J. H. Fan, C. M. Chong, *Mater. Today Nano* **2022**, *17*, 100162.

[7] J. Wang, C. H. Gao, Z. Yang, M. Zhang, Z. L. Li, H. L. Zhao, *Carbon* **2022**, *192*,

277.

[8]    Q. Liu, Y. X. Ji, X. M. Yin, J. W. Li, Y. J. Liu, X. Hu, Z. H. Wen, *Energy Storage Mater.* **2022**, *46*, 384.

[9]    Q. Ma, Z. Q. Zhao, Y. Zhao, H. W. Xie, P. F. Xing, D. H. Wang, H. Y. Yin, *Energy Storage Mater.* **2021**, *34*, 768.

[10]   J. Wang, Z. Yang, B. G. Mao, Y. X. Wang, Y. Jiang, M. H. Cao, *ACS Energy Lett.* **2022**, *7*, 2781